Institute of Earth and Environmental Sciences

Thesis in cumulative form entitled:

Landslide kinematics and interactions studied in central Georgia by using synthetic aperture radar interferometry, optical imagery and inverse modeling

Dissertation

To obtain the academic degree

"doctor rerum naturalium" (Dr. rer. nat.)

for the scientific discipline " Geophysics "

submitted to

the Faculty of Mathematics and Natural Sciences

at the University of Potsdam

Elena Nikolaeva

Potsdam, October 2013

I herewith declare that the work in this present thesis is my own work without any help from third parties and without the use of any aids beyond those given. The thesis consists no material previously published by another person.

This work has not been submitted in Germany or abroad to any other examination board in this or similar form.

Potsdam 28 October 2013

Elena Nikolaeva

"You are never given a dream without also being given the power to make it true. You may have to work for it, however."

Richard Bach

"*Не приучайся легко падать. Ибо при каждом падении обрушивается крепостная стена души, и вход для врага делается все более свободным, пока он окончательно не сделает побежденного пленником*".

старец Иосиф Исихаст

Acknowledgements

work on Skype, for their sustained support me during stressful period, for their wise advices and for their faith in me. I am grateful to my nieces that they remember me and have always enjoyed our virtual or real meetings.

Contents

Abstract

Landslides are one of the biggest natural hazards in Georgia, a mountainous country in the Caucasus. So far, no systematic monitoring and analysis of the dynamics of landslides in Georgia has been made. Especially as landslides are triggered by extrinsic processes, the analysis of landslides together with precipitation and earthquakes is challenging.

In this thesis I describe the advantages and limits of remote sensing to detect and better understand the nature of landslide in Georgia. The thesis is written in a cumulative form, composing a general introduction, three manuscripts and a summary and outlook chapter.

In the present work, I measure the surface displacement due to active landslides with different interferometric synthetic aperture radar (InSAR) methods. The slow landslides (several cm per year) are well detectable with two-pass interferometry. In same time, the extremely slow landslides (several mm per year) could be detected only with time series InSAR techniques. I exemplify the success of InSAR techniques by showing hitherto unknown landslides, located in the central part of Georgia. Both, the landslide extent and displacement rate is quantified.

Further, to determine a possible depth and position of potential sliding planes, inverse models were developed. Inverse modeling searches for parameters of source which can create observed displacement distribution. I also empirically estimate the volume of the investigated landslide using displacement distributions as derived from InSAR combined with morphology from an aerial photography. I adapted a volume formula for our case, and also combined available seismicity and precipitation data to analyze potential triggering factors. A governing question was: What causes landslide acceleration as observed in the InSAR data?

The investigated area (central Georgia) is seismically highly active. As an additional product of the InSAR data analysis, a deformation area associated with the 7th September Mw=6.0 earthquake was found. Evidences of surface ruptures directly associated with the earthquake could not be found in the field, however, during and after the earthquake new landslides were observed. The thesis highlights that deformation from InSAR may help to map area prone landslides triggering by earthquake, potentially providing a technique that is of relevance for country wide landslide monitoring, especially as new satellite sensors will emerge in the coming years.

Zusammenfassung

Erdrutsche zählen zu den größten Naturgefahren in Georgien, ein gebirgiges Land im Kaukasus. Eine systematische Überwachung und Analyse der Dynamik von Erdrutschen in Georgien ist bisher nicht vorhanden. Da Erdrutsche durch extrinsische Prozesse ausgelöst werden, wird ihre Analyse zusammen mit Niederschlag und Erdbeben zu einer besonderen Herausforderung.

In dieser Dissertation beschreibe ich die Potenziale und Limitierungen der Fernerkundung für die Detektion und das Verständnis von Erdrutschen in Georgien. Die Arbeit ist in einer kumulativen Form geschrieben, und besteht aus einer allgemeinen Einführung, drei Manuskripten sowie einer Zusammenfassung und einem Ausblick.

In der vorliegenden Arbeit, Gestimme ich die Oberflächenverschiebung von aktiven Erdrutschen mit Methoden der Radarinterferometrie (InSAR). Die langsamen Erdrutsche (cm pro Jahr) konnten im einfachen Vergleich zeitlich unterschiedlicher Radaraufnahmen (two-pass InSAR), gut nachgewiesen werden. Die extrem langsamen Erdrutsche (mm pro Jahr) konnten hingegen nur mit InSAR Zeitreihentechniken nachgewiesen werden. Der Erfolg der angewandten InSAR Techniken wird durch die erfolgreiche Identifikation von bisher unbekannten Erdrutschen in Zentral Georgien veranschaulicht. Sowohl das Ausmaß als auch die Verschiebungsrate der Erdrutsche wurden quantifiziert.

Ferner, um die mögliche Tiefe und Lage von potentiellen Gleitflächen zu bestimmen, wurden inverse Modelle entwickelt. Inverse Modellierung sucht nach Parametern der Quelle, welche die beobachtete Verschiebungsverteilung reproduzieren können. Ferner habe ich anhand der ermittelten Verschiebungsverteilung aus InSAR in Verbindung mit der Morphologie aus Luftaufnahmen das Volumen der untersuchten Erdrutsche empirisch abgeleitet.

Ich habe eine Volumenformel für unseren Fall angepasst, und die verfügbaren Datensätze bezüglich Seismizität und Niederschlag kombiniert, um potenzielle auslösende Faktoren zu analysieren. Eine leitende Frage hierbei war: Was sind die Ursachen für die Beschleunigung von Erdrutschen, wie sie in den InSAR Daten beobachtet werden konnte?

Das Untersuchungsgebiet in Zentral Georgien ist seismisch sehr aktiv. Als zusätzlichen Produkt der InSAR Datenanalyse wurde ein Deformationsgebiet gefunden, welches im Zusammenhang mit dem Mw=6.0 Erdbeben vom 7. September 2009 zusammenhängt. Beweise für Oberflächenbrüche, die direkt mit dem Erdbeben zusammenhängen, konnten in dem Gebiet nicht gefunden werden, jedoch konnten während und nach dem Erdbeben neue Erdrutsche beobachtet werden. Die Dissertation unterstreicht, dass Verformungsinformationen aus InSAR Analysen helfen können ein Gebiet, welches von Erdbebeninduzierten Erdrutschen gefährdet ist, zu kartieren. Potenziell stellt InSAR eine Technik dar, die von Bedeutung für die landesweite

Überwachung von Erdrutschen sein kann, insbesondere im Hinblick auf die neuen Satellitensensoren, die in den kommenden Jahren verfügbar sein werden.

1. Introduction

1.1. Motivation

1.1.1.   State of Art

In recent decades, the number of landslide studies has tremendously grown, with one aim of decreasing the social and economic damage caused by them. The reasons for landslides include growing urbanization and the associated development and deforestation in landslide-prone areas (Turner and Schuster 1996). Also, the increased regional precipitation due to changes in weather conditions, tectonic activity and volcano eruptions play major roles in this phenomenon (Thuro et al. 2010).

In connection with this problem, landslide detection and mapping projects have been set up in a number of countries. Optical and radar remote sensing data are widely used for landslide detection and monitoring (Tofani et al. 2013). However, until now, field surveys have been essential for identifying and qualifying landslides, as they are useful for investigations at the local scale and known landslides. Nevertheless, optical and radar imagery have proven to be superior, and lower-cost techniques than field surveys for covering wide spatial and temporal scales for detecting and mapping landslide (Tofani et al. 2013).

Some slopes have the potential to fail catastrophically and produce huge, rapidly moving mass movements that can be destructive, but identifying such slopes can be difficult with standard ground truth observations. In addition to this, the monitoring of landslides is not widely possible with ground based tools, due to economic reasons and only a few hazardous landslides are monitored permanently (Thuro et al. 2010). However, in this case, radar remote sensing techniques also are widely used for monitoring landslide as part of early warning systems (Tofani et al. 2013).

1.1.2.   Study area

There are several landslide-prone regions in the world where very little efforts have been made to monitor landslides and consequently no detailed landslide inventory map exists, which is inherent for natural hazard studies. One of the most landslide susceptible areas and one that has not been studied in details is central Georgia (van Westen et al. 2012). This region is very mountainous and

tectonically active, with most moderate and large earthquakes accompanied by landslides, which contribute a significant proportion of the total earthquake damage (Jibson et al. 1994).

The effects of earthquake shaking on slope stability are not limited to the short period of actual shaking. In some cases, landslides have begun to move hours or even days after an earthquake (Jibson et al. 1994). Accordingly, monitoring and early warning may prevent human losses in those situations. Also, landslides initially triggered by an earthquake can be reactivated as a result of other factors, e.g., heavy precipitation.

We studied the Sachkhere area (Fig. 1.1), located in the seismically active central Georgia region, which is also susceptible to landslides. The results will help to improve upon our understanding of the physics of landslides and the capability of the employed methods. The study area also includes the epicenter of the last big earthquake (Mw=6.0) in central Georgia, which may have accelerated landslides.

Fault structures in Georgia (Gamkrelidze and Shengelia 2007) exist mainly at the boundaries of tectonic units. The majority of deep faults are hidden (the fault surface does not reach the earth surface) and their features can be revealed based on structural, magmatic, sedimentary, remote sensing, borehole and
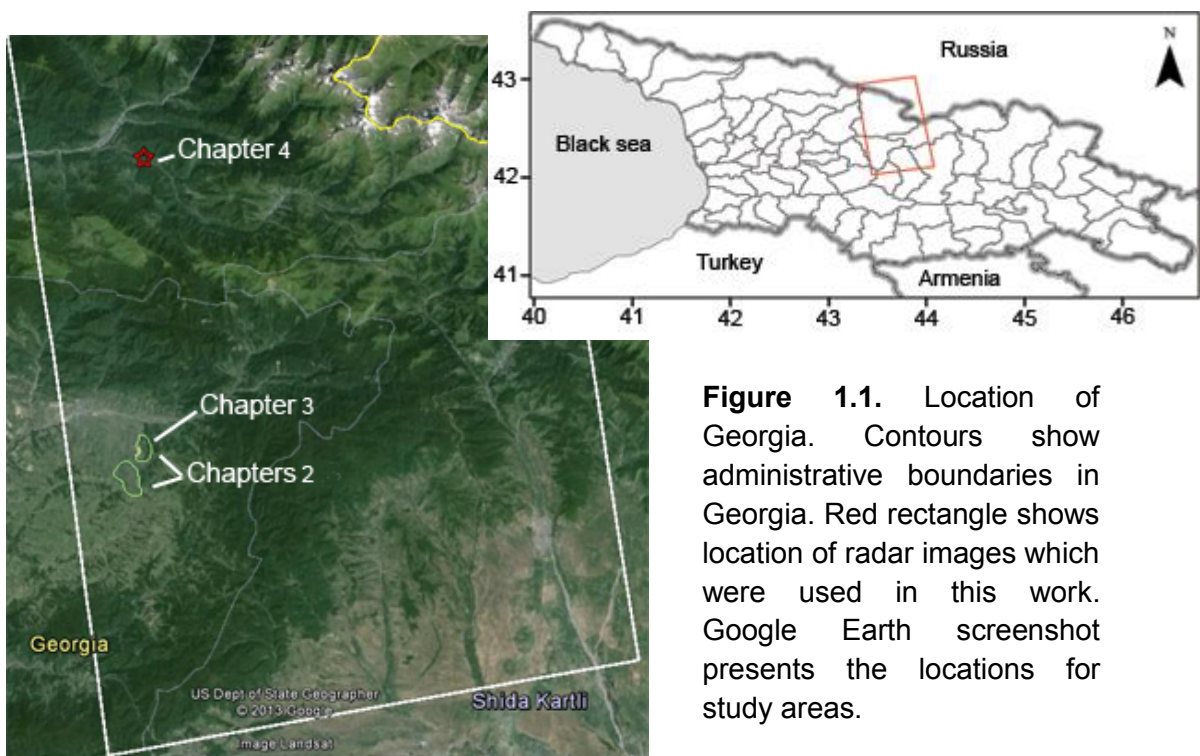
Figure 1.1. Location of Georgia. Contours show administrative boundaries in Georgia. Red rectangle shows location of radar images which were used in this work. Google Earth screenshot presents the locations for study areas.

other geological and geophysical (e.g. gravimetric, magnetic, seismic, deep seismic sounding) data (Reilinger et al. 2006; Adamia et al. 2010). These literature data help to better understand the appearance of the studied landslides.

The landslide inventory map in Georgia is based on field observations and optical image mapping. For the first time, this work used the interferometric synthetic aperture radar (InSAR) techniques for landslide mapping in Georgia have been found. Landslides detected and analyzed within the framework of this thesis have not been previously identified. The investigation of landslides in central Georgia may therefore proceed a re-assessment of the existing landslide inventory information, and give a future perspective of the InSAR techniques for whole Caucasus area.

1.1.3.   Research objectives

The study involves two main research fields, first the application and comparison of different radar interferometry remote sensing methods to map landslides, and second the quantification of the dynamics of landslides to obtain an improved understanding of landslide processes with respect to this previously unstudied area. Further discussion on the effect and detection of a landslide follows these two parts, both of which have formed peer reviewed articles accepted for publication.

We have formulated several method objectives. As there are different InSAR techniques available, a significant task was to find the methods from frequently used InSAR techniques which can detect and monitor landslides display a range of velocities and displacements. Also, we applied remote sensing tools to central Georgia poorly or notatall monitored landslide areas to improve the regional landslide inventory map. Compare and identify correlation between the InSAR results and an aerial image, a field observation. The aim is to test InSAR method capabilities to detect landslide area in particular target area.

The aspects of this project focusing on landslide dynamics are:

- What are the dimensions and velocities of the landslides?
- How does displacement relate to surface fractures observed?
- Extraction of possible triggering factors, such as rainfall, an earthquake and mining activity.

- Development of the existing method for an evaluation of the landslide volume for a complex case (translational-rotational landslide).
- Derive important landslide parameters (velocity, landslide activity, volume) relevant for assessing the hazard potential.

The combination of technical and process-oriented research allowed for the formulation of a thesis / concept that can also be adapted to other regions as well.

1.2. Methodologies

This thesis not only makes use of different InSAR methods, but also combines such techniques with aerial photography, supported by field inspections. In the following, we provide a short introduction of each method, more details of which are presented in the individual publications.

1.2.1.   InSAR

The Synthetic Aperture Radar (SAR) interferometry method is the basis for other techniques (stacking, PS, SBAS) which have been exploited in this thesis. The details for the other methods are outlined in the next chapter. The basis of the InSAR method is described herein.

A radar observation system sends short powerful pulses to the ground and receives the reflected waves, and records the amplitude and phase of the backscattered signal from the surface. This means that the round-trip time between the radar and the ground observation can be measured. This implies the phase difference between two SAR acquisitions from the same target can be calculated. Therefore, the change in the location of an observable target area on the surface is detected by using information derived from the radar wavelength and the relative phase change. Thereby, phase values contain information about the stability of the Earth's surface. Changes in the reflectivity of the ground, in the viewing perspective and atmosphere affects on the radar signals may introduce errors to any results (Tarayre and Massonnet 1994).

Temporal decorrelation or changes in reflectivity mostly come from variations in the ground's moisture content or vegetation (Wei and Sandwell 2010). Baseline decorrelation or different viewing geometries are due to different satellite positions from one satellite pass to the next (Zebker and Villasenor 1997). Phase adjustments are made on the basis of orbital information of satellite

positions. Additional phase shifts in interferogram may appear due to the atmosphere (Zebker et al. 1997). This effect can be isolated from a time series of interferograms or based on topography correlated atmospheric delay. Based on the above, the interferometric phase difference $\Delta\varphi_{total}$ between two corresponding points may be presented as:

$$\Delta\varphi_{total} = \Delta\varphi_{ref} + \Delta\varphi_{topo} + \Delta\varphi_{defo} + \Delta\varphi_{atmo} + \Delta\varphi_{noise} \ (1.2.1)$$

Where $\Delta\varphi_{ref}$ is a reference phase caused by the Earth curvature, and is sensitive to slightly different viewing positions of satellites. Phase contribution $\Delta\varphi_{topo}$ is from topography and can be removed by an appropriate Digital Elevation Model (DEM). Component of phase $\Delta\varphi_{defo}$ presents a possible deformation. Phase contribution $\Delta\varphi_{atmo}$ is significant when different atmospheric conditions arise between acquisitions. Phase noise $\Delta\varphi_{noise}$ may appear due to temporal changes in the scatterers, different look angle and thermal conditions, the Doppler Centroid effect, volume (scattering medium) and processing (image pre-processing).

This distance or displacement is one dimensional projection in the line-of-sight (LOS). The LOS angle depends on the satellite and on the acquisition parameters. Thus, the observed movement relates to the position of the satellite and includes vertical and horizontal components. It is a challenge to distinguish the vertical and horizontal components from InSAR signal. However, the additional ground information may help to evaluate vertical and horizontal components.

1.2.2. Aerial photograph interpretation

Aerial photographs are commonly used in landslide mapping. High resolution aerial photography interpretation allows for the detection of landslide related fractures, analysis of which leads to the inference of the mechanisms involved.

The identification and interpretation of a landslide-related fracture is based on the difference in texture, brightness, pattern and shapes (Walstra et al. 2007). This difference appears due to the different reflective parameters of the objects. The reflection from an object depends on its physical and chemical characteristics, changes in its form, and the position or appearance of the topographic surface.

The main aim of aerial photography interpretation in this thesis is to map morphological features related landslides that show relationships between the various landscape elements, the distributions of vegetation and of soil moisture conditions.

1.2.3. GIS analysis

We collected and analysed all data in a Geographical Information System (GIS). The considuration of thematic layers help to take into account several parameters for the study area at the same time. The results from InSAR, extracted contours from the digital representation of a topographic surface and aerial images were loaded into the GIS system (ArcGIS) and their analysis revealed relationships between displacement signals and other field observations.

1.2.4. Modeling

Modelling of the physical processes related to landslides can help to predefine the more important physical parameters from simplified version of the real process. We used an analytical homogeneous elastic half-space model (Okada 1985) to predict surface displacements due to a source, defined as a finite rectangular fault at depth. The model uses the following fault parameters: dimensions (length and width), location, orientation (strike and dip) and the offset on the fault.

We used InSAR observation data to make as realistic model as possible. The inverse problem is a procedure to extract the parameters of an analytical model from an observed displacement field. The InSAR observation data were inverted to generate synthetic data, and based on this, estimate the geometry and location of the landslide's sliding surface. This is composed to geometric models, to inter the volume of a landslide, which is of relevance for understanding the dynamics and assessing associated hazards.

We therefore developed on Okada model to simulate the 7th September 2009 earthquake in Racha, central Georgia. We obtained synthetic surface displacement data by using the focal mechanism parameters of the earthquake and compared these with observations.

1.3. Thesis organization

This thesis is written cumulative form and divided into four chapters. Two Chapters 2 and investigate the technical potential of different InSAR methods for detecting to detect landslides in central Georgia. Chapter 4 focuses on the analysis of one landslide, with the purpose of developing a procedure to extract the physical and kinematic parameters of landslides by using remote sensing and inverse modeling. Chapter 5 analyses Racha 2009 earthquake, investigating the spatial relationship between the occurrence of the deformation induced by the earthquake and contemporary sliding events. Each chapter contains an indepth introduction and discussion section, and is equivalent to one publishable manuscript, out of which all but one have been published or have been submitted at the time of this writing. The thesis ends with an overall summary and outlook, placing each chapter within the appropriate contest. .

1.4. Chapter summaries

Chapter 2: The chapter entitled "Detection and mapping of landslides in central Georgia, Caucasus: a comparison of different InSAR methods" describes the use of different InSAR processing techniques (including stacking) for landslides. The results show that success depends on data and method selection.

This chapter has been submitted to the IEEE Journal of Selected Topics in Applied Earth Observations and Remote Sensing (JSTARS-2012-00600.R2) for possible publication. Copyright may be transferred without notice, after which this version may no longer be accessible.

Author contributions: Nikolaeva processed the interferograms, the stack, the InSAR time series datasets, mapped active areas. The analyses of the InSAR results were made by Nikolaeva and Walter. Nikolaeva wrote the manuscript under the supervision of Walter.

Chapter 3: The chapter entitled "Landslide observation and volume estimation in central Georgia based on L-band InSAR" describes the analysis and results in a stepwise approach to detect and monitor landslide. We estimate important parameters such as landslide velocity, active area and landslide volume based on radar remote sensing observations, Geographic Information Systems (GIS) applications and inverse modeling.

This chapter was published in Natural Hazards and Earth System Sciences (NHESS).

Author contributions: Nikolaeva processed the interferograms, and mapped the landslide fractures during a field trip. The analyses of the InSAR results were made by Nikolaeva and Walter. Walter, Shirzaei and Zschau shared discussions with Nikolaeva about the modeling of the landslide with an Okada model. Shirzaei provided an inversion code. Nikolaeva expanded a concept of the calculation of the rotational landslide volume. Nikolaeva wrote the manuscript under the supervision of Walter.

Chapter 4: The chapter entitled "Did InSAR detect co-seismic (post-seismic) deformation in Racha region, Georgia?" describes the key role of seismic activity in the landslide prone area and shows the surface deformation detectable by InSAR possible due to the 7 September 2009 earthquake in the central Georgia.

The chapter is planned for publication in Geophysical Research Letters.

Author contributions: Nikolaeva processed the interferograms, built a model. Nikolaeva analyzed the dataset with the collaboration of Walter and Nikolaeva wrote the manuscript under the supervision of Walter.

2. Detection and mapping of landslides in central Georgia, Caucasus: a comparison of different InSAR methods

E.Nikolaeva[1], T.R. Walter[1]

[1]Department 2 - Physics of the Earth, Helmholtz Center Potsdam – GFZ
German Research Center for Geosciences, Potsdam, Germany

Abstract

Interferometric synthetic aperture radar (InSAR) methods have been shown to be particularly useful in the detection and monitoring of landslides. We compared results obtained from four widely used InSAR methods: two-pass interferometry, a stacking process, persistent scatterer interferometry (PS-InSAR) and the small baseline subset (SBAS) approach. We applied these to twelve radar images acquired by the ALOS (PALSAR) satellite over central Georgia, in the Caucasus region of Eurasia. For the given dataset and scenario, we were able to detect various landslides properly only by applying a combination of InSAR methods. We show that the application of different InSAR methods to the same input data produced different combinations of data and hence different noise levels, pixel selections, detection thresholds and results. We also compared our results to aerial photography and field observations to test the theory that the success of each method depends on the landslide velocity, the landslide direction and the associated decorrelation. We studied two landslides in detail. We describe their geometry and displacement rates, along with the relevant wider implications of using InSAR methods in landslide research.

Index Terms – landslide displacement, InSAR time series, Georgia, surface displacement, geodetic monitoring

2.1. Introduction

Over the last decade, remote sensing techniques have increasingly contributed to the detection and monitoring of subaerial landslides. Commonly, photogrammetry methods are used to quantify and determine these subaerial mass movements. In addition, interferometric synthetic aperture radar (InSAR) techniques have been used increasingly for landslide detection and monitoring

(Colesanti et al. 2003b; Colesanti and Wasowski 2006; Biescas, E., Crosetto, M., Agudo, M., Monserrat, O., and Crippa 2007; Perski et al. 2009; Perissin and Wang 2011; Bovenga et al. 2012). The limitations of the various InSAR techniques become evident when they are used for landslide detection and monitoring. InSAR techniques are particularly sensitive to the velocity and direction of displacements and to signal decorrelation induced by vegetation cover, steep topography (layover, shadow effects), satellite orbits, temporal decorrelation and other factors. Therefore, our strategy was to compare the different processing approaches available that may enhance the effectiveness of landslide detection and monitoring and further improve understanding of landslide behavior (Bulmer et al. 2006; Colesanti and Wasowski 2006).

A variety of studies have described the use of different InSAR techniques in combination, with a focus on landslides that fall into the categories of extremely slow and slow slope displacements (Bulmer et al. 2006; Biescas, E., Crosetto, M., Agudo, M., Monserrat, O., and Crippa 2007; Xia 2008) of a few mm per year to several cm per year, respectively (Petley et al. 2005), (Varnes 1978). Extremely slow displacements have been investigated for instance using the two-pass InSAR method (Biescas, E., Crosetto, M., Agudo, M., Monserrat, O., and Crippa 2007) and using PS (Permanent Scatterer) (Perski et al. 2009). The two-pass InSAR method has been applied to the measurement of slow displacement phenomena (Bulmer et al. 2006; Biescas, E., Crosetto, M., Agudo, M., Monserrat, O., and Crippa 2007; Perski et al. 2009). However, the use and comparison of different InSAR methods has not been common in research to date, even though such comparisons are important to understanding landslide hazards. As this paper shows, improving the detection of landslides in central Georgia required consideration of multiple processing methods.

Accurate detection of landslides is necessary to minimize the associated negative impacts, damage and fatalities. It is necessary to monitor landslides to protect local populations, water sources and infrastructure. InSAR, which is a tool for detecting and monitoring landslide velocities, can be used to measure the acceleration of a landslide. Therefore, InSAR methods may potentially be used as early warning systems for landslides (Thiebes 2012).

We show in this paper that locations that display clear landslide deformation signals in two-pass interferometry may decorrelate with the application of a time series method. We describe the target area in central Georgia, in the Caucasus region of Eurasia, the ALOS dataset and the methods investigated. We then compare the results of the stack process to the results obtained using two-pass

InSAR, PS and SBAS and perform a quantitative validation of landslide occurrence using optical imagery.

2.2. Test area and methods

2.2.1.   Central Georgia

Central Georgia, in the Caucasus region of Eurasia, contains active tectonic faults, fractures (Edilashvili et al. 1974; Gamkrelidze and Shengelia 2007) and landslides (Jibson et al. 1991), (Jibson et al. 1994). The Caucasus region is considered a landslide and avalanche hazard hotspot (Arnold et al. 2006). When climate, lithology, earthquake activity, topography and land cover are considered in the context of the global occurrence of natural disasters (Arnold et al. 2006), Georgia is considered a zone of medium to high landslide hazard and the highest possible level of avalanche hazard.

Our study focuses on the Imereti region in the Sachkhere district (Fig. 1), where most of the sediments that are prone to sliding processes correspond to the sandstones and sands of the area (Edilashvili et al. 1974). Landslides in the Sachkhere district threaten villages and can dam rivers (Fig. 1) and affect major quartz sand mining areas (Fig. 1) that have been active for decades. In addition to geology, topography and rainfalls, earthquakes may be an important triggering mechanism in this area. For example, on 29 April 1991, an earthquake (Ms=7.0) reactivated existing landslides and triggered new ones (Jibson et al. 1991), some of which were more than 30 km from the epicenter (Jibson et al. 1994).
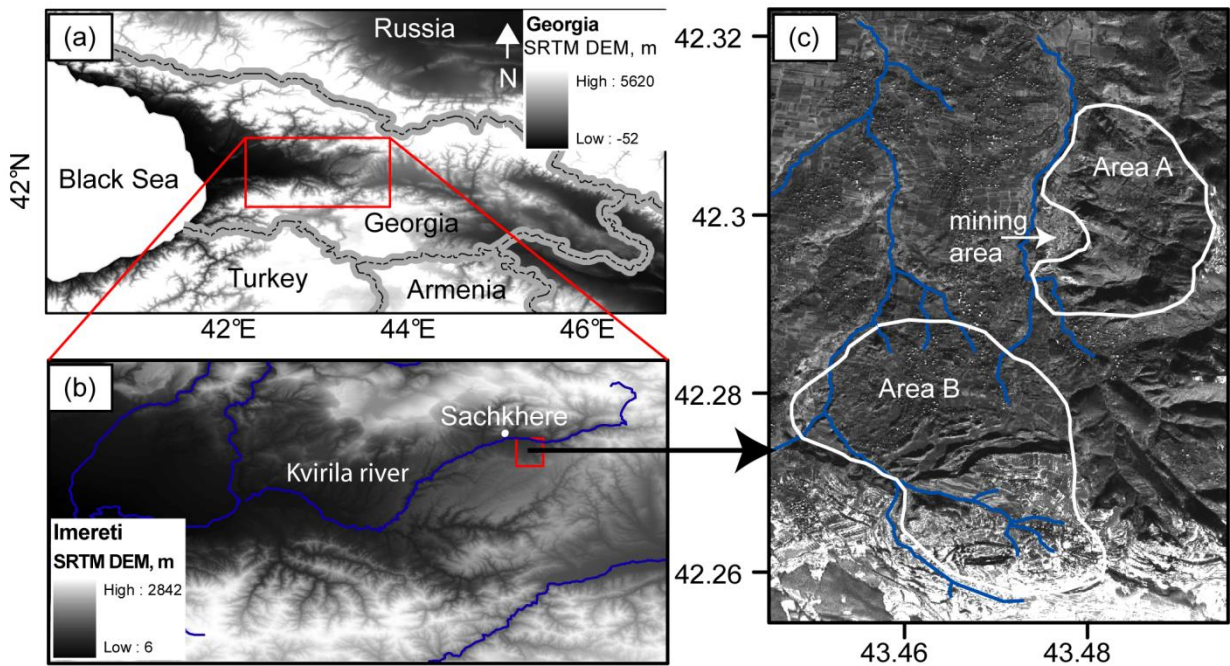
Figure 2.1. Study area in Georgia, Caucasus. (a) Georgia is covered by an SRTM digital elevation model. The red box shows the Imereti region. (b) The small red box shows the investigated area in the Sachkhere district. (c) Optical QuickBird panchromatic imagery at 0.6-meter resolution, acquired in December 2007. The contours show the proposed boundaries of landslide area A and area B. The blue lines are rivers (b) and streams (c).

Despite the known landslide hazard, there is no monitoring program in existence to study the dynamics of selected landslides in Georgia. InSAR techniques may be very useful for landslide mapping and monitoring. The main advantages of these techniques are their wide coverage, their high spatial resolution and their usefulness in investigating areas that are difficult to access at low cost.

Unfortunately, neither GPS data nor any other types of monitoring data (e.g., rainfall, displacement) were available for this region. Many other landslide regions in Georgia are not monitored by geodesy either. Therefore, our study constituted a test of the InSAR techniques that may be useful in the detection and monitoring of landslides in Georgia in the future.

2.2.2. Data and Methods

We selected all of the radar images acquired by the ALOS PALSAR (phased array type L-band synthetic aperture radar) satellite over our study area in central Georgia. The resolutions of SAR images are 4.8 m and 4.5 m in the slant range and azimuth direction, respectively. In total, 16 images, spanning the

period from July 2007 to June 2010, were available from the JAXA archive. As the available acquisitions are from ascending orbits only (where observations are made from westward-looking direction), this study was restricted to a single viewing geometry. No descending data were available. We created pairs of interferograms, however, and found that pairs that included the radar images (denoted in year.month format) 2007.01, 2007.02, 2009.01 and 2010.03 exhibited strong decorrelation due to meteorological conditions, even for combinations with short spatial and temporal baselines. Therefore, these images were not used in this study. We also obtained and analyzed radar data from C-band satellites (ERS1/2, Envisat) but found them unsuitable due to the level of decorrelation noise.

The ALOS PALSAR radar raw data were processed into single-look complex (SLC) images using the ROI_PAC (Repeat Orbit Interferometry Package) software (Rosen et al. 2004). We focused our research on a local region where a deformation signal was observed in the interferograms. We processed the radar images corresponding to an area of 30 km². The selection of such a small area enabled us to reduce the effect of atmospheric phase delay (APD) and to improve image co-registration.
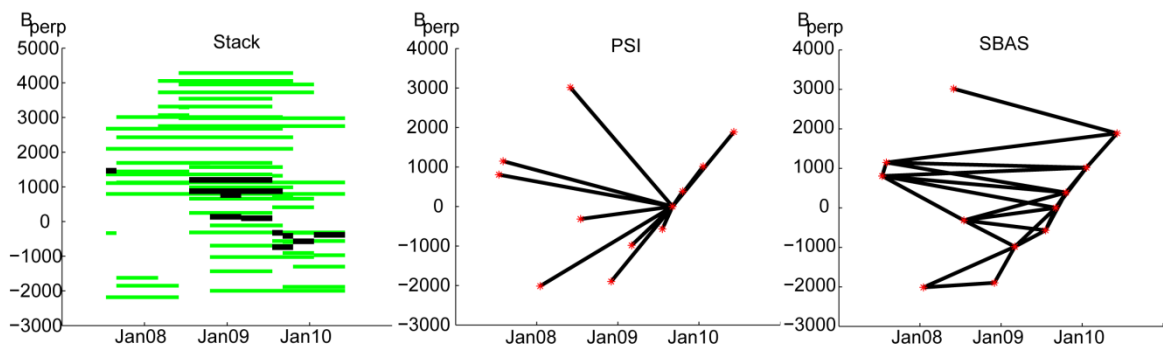
Figure 2.2. Baseline plot for (a) InSAR two-pass interferometry; the black lines show interferograms that were successfully unwrapped, (b) the persistent scatterer method; the point to which all are pulled is a reference (master) and (c) the small baseline approach. The lines represent pairs of interferograms, and the beginning and end of a line represents a SAR image. All methods used twelve images only, but the number and combination of pairs created and the pixels selected may differ. See the text for details.

The ASTER GDEM (Global Digital Elevation Model) was used to subtract the topography from each interferogram. The ASTER GDEM is based on matches of optical images with grid sizes of 30 m. The ASTER GDEM has been found to

be more accurate for mountainous areas than SRTM DEM data with a resolution of 90 m (Jacobsen 2010).

We applied four methods to the processing of the ALOS PALSAR dataset and compared the outcomes. Pairs of interferograms were selected for each of the methods described below (Fig. 2). The four methods we investigated were the following:

1) Two-pass interferograms—We processed radar images using two-pass interferometry (Rosen et al. 2000), (Massonnet and Feigl 1998) (Fig. 2(a)). Two-pass interferometry involves generating an interferogram from two radar images obtained at different times. An interferogram describes the difference in the phase of the waves returning to the satellite (Massonnet and Feigl 1998). The Delft Object-Oriented Interferometric Software (DORIS) (Kampes and Usai 1999) was used to create the two-pass SAR interferograms (Massonnet and Feigl 1998). A multilook factor, two pixels in range and four pixels in azimuth direction, was applied to reduce the phase noise in the interferograms. Consequently, the output InSAR images have a spatial resolution of approximately 15 m in both directions. To reduce the atmospheric noise in the InSAR data, the interferograms were filtered using a gamma filter, as described in (Principe et al. 1993). To remove the contribution of orbital errors to the signal, a wavelet multi-resolution analysis and robust regression were used (Shirzaei and Walter 2011). The corresponding wrapped phase values were unwrapped, using the branch-cut phase unwrapping algorithm (Goldstein and Werner 1998a) (Fig. 3, first six interferograms) and SNAPHU (Statistical-Cost, Network-Flow Algorithm for Phase Unwrapping) (Chen and Zebker 2001; Chen and Zebker 2002) (Fig. 3, last six interferograms), to high-quality InSAR displacement maps.

2) *Stacking process*—Eleven interferograms were successfully unwrapped (Fig. 2(a), black lines) and were used further in this study. We started with the phase values of the eleven interferograms and co-registered all. We then unwrapped them, calculated the displacement velocity for each interferogram and averaged these values. The output from this stacking process was an average velocity over the whole period (2007.07–2010.01), with atmospheric phase components reduced (Zebker et al. 1997). We stacked the velocity maps based on the assumption that the displacement had a constant rate.

In addition to the two-pass and stacking methods, we also investigated the area using InSAR time series. Time series data makes it possible to select high-quality pixels and apply spatial-temporal filters to reduce noise levels. We used

the StaMPS software (Ferretti et al. 2001; Hooper 2009) for these processing steps, to compare the Persistent Scatterers (PS) and Small BAseline Subset (SBAS) methods.

3) *Persistent Scatterers*—The PS method is based on analysis of stable pixels, which are also called persistent scatterers (Ferretti et al. 2001). Acquisitions were co-registered and re-sampled to the same reference image (master). Interferograms were computed between eleven slave images and the master image (Fig. 2(b)). The first selection of potential PS points was based on a coherence threshold (Hooper 2004).

4) *Small BAseline Subset*—The SBAS method is based on combining radar images with small perpendicular and temporal baselines to reduce spatial phase decorrelation (Berardino et al. 2002).

The initial steps of StaMPS are the same as those for the PS and SBAS processes. The pixel selection process occurs after data loading and the estimation of the phase noise and is based on noise characteristics. The PS weeding step drops pixels whose minimum standard deviation is greater than a given threshold. The next steps are phase correction and unwrapping. In the SBAS process, the phase values are restored with respect to the original master image using least-squares inversion. In the last step, the spatially correlated errors in the DEM are calculated and the atmosphere and orbit error phase is estimated.

2.2.3. Differences in interferogram selection

Twelve images were used for all methods. Because of the processing procedure and the pair selection criteria, the number of interferograms differs by method. The methods considered differ from each other not only in terms of the information content but also in terms of the interferogram and pixel selection criteria. Therefore, we expected slightly different results. The interferograms were selected as follows. First, we created 44 interferograms using the twelve radar images, based on the selection criteria (Fletcher 2007). The pairs have perpendicular baselines of 2,000 m which is critical for ALOS PALSAR (Furuya 2010), and maximum temporal baselines of up to 2. 5 years. We selected the eleven best interferograms with coherence levels greater than 0.4 that we could unwrap and use in the stack process (Fig. 2 (a), black lines). We excluded the 2009.09.04–2010.01.20 (year.month.day) interferogram (Fig. 3) due to strong decorrelation. We unwrapped the remaining eleven interferograms to determine

the displacement.

For PS, we chose the master image 2009.09.04 on the basis of minimization of perpendicular baselines (Fig. 2 (b)). Such a choice increases the amplitude stability of pixels for the whole set of images (Ferretti et al. 2001).

The data selection was somewhat different for the SBAS process. We used a threshold for the spatial and temporal baselines in an attempt to reduce the spatial and temporal decorrelation (Berardino et al. 2002). We found that the interferograms were noisy, with perpendicular baselines greater than 1,700 m. Therefore, we chose a perpendicular baseline limit of 1,700 m, which is less then critical (Furuya 2010). A shorter baseline threshold would make image pairing difficult, due to the limited number of images in the dataset. As the quality of InSAR images was good over time, spanning more than one year (460 days) between the acquisitions, we were able to include interferograms with longer temporal baselines in the SBAS process. Figure 2 (c) shows the 21 pairs of interferograms that were computed using our baseline threshold.

In all cases, the results were calibrated with respect to an area in the northwestern part of the image that was assumed to be stable.

We also employed aerial photography with a resolution of 0.6 m for validation and for a land cover analysis conducted using a geographic information system (ArcGIS).

2.3. Results from InSAR, PS and SBAS

The ground displacements within an area 4.16 km wide (west to east) and 6.85 km long (north to south) are related to areas A and B outlined in Figure 1 and were measured using all four methods considered. Two-pass interferograms show a clear phase shift (observable as a colorful pattern in Fig. 3) with short temporal baselines (45–180 days) and a decorrelation from interferograms with large temporal baselines (Fig. 2 (a), green lines). The interferograms depict a significant displacement area with dimensions of 2 km from north to south and 0.5 km from west to east. We refer to this area as landslide A (Fig. 4 (a), area A).
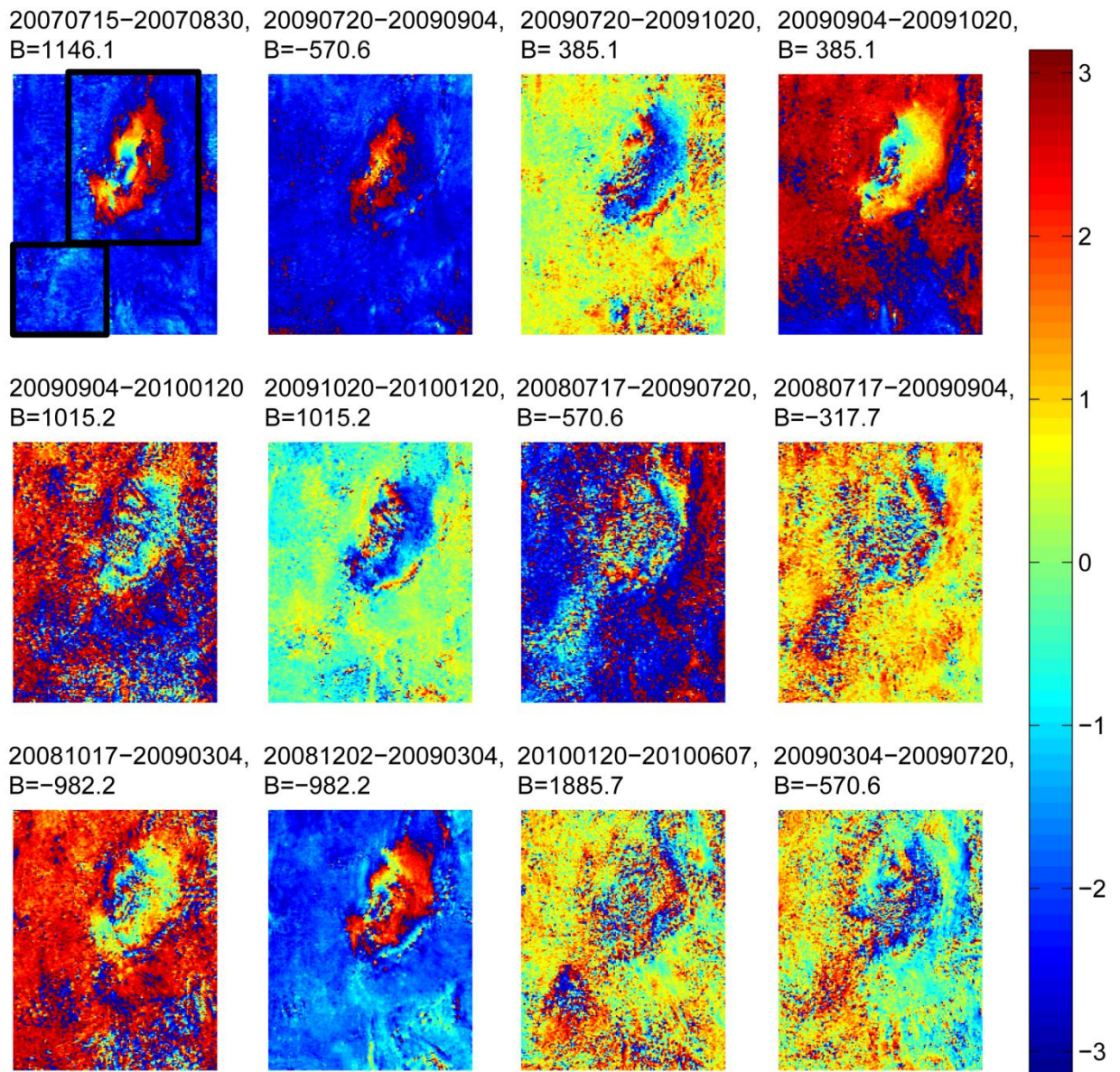
Figure 2.3. Examples of wrapped interferograms (radian) in radar coordinates. A signal of deformation is clear for area A (upper black box in upper left corner interferogram) in all interferograms. The signal from area B (lower black box in upper left corner interferogram) appears in the interferograms with long temporal baselines, but not in all interferograms.

Displacement in the range of 30–80 mm in the line of sight (LOS) was observed in each interferogram. The displacement in area A is visible in interferograms with different master–slave combinations. The shift in phase is traced in each independent interferogram. The results from the stacking process show an appreciable displacement pattern in area A (Fig. 4 (a)). Positive and negative signs indicate observed LOS movement toward and away from the satellite,

respectively. In this case, almost all of the displacement is toward the satellite (shown by the warm colors in Fig. 4).
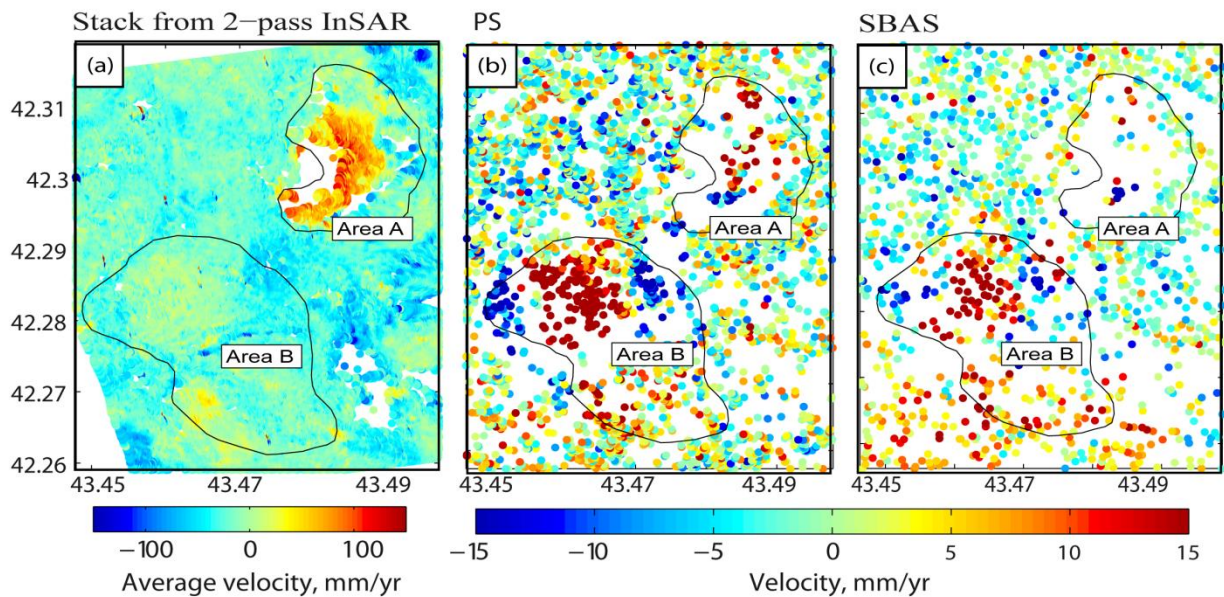
Figure 2.4. (a) The stack velocity (mm/yr) in the LOS direction was calculated using eleven two-pass interferograms (see Fig. 3, excluding interferogram (year.month.day) 2009.09.04–2010.01.20 due to strong noise). (b) PS results, LOS velocity (mm/yr). (c) SBAS results, LOS velocity (mm/yr). Note that the velocity scales for area A and area B differ by approximately one order of magnitude.

The results obtained using the PS and SBAS methods, shown in Figures 4 (b) and (c), indicate that the landslide area A largely lacks coherence. There are several pixels from the PS and SBAS processes in area A (Figs. 4 (b), (c)); however, they were found to be isolated from each other and therefore not unwrapped reliably.

Another displacement area (area B) stood out less than 1 km to the south of area A (Figs 4 (b), (c)). The LOS range of displacement is generally about ±15 mm/yr for both the PS and SBAS methods (Figs. 6(a), (d)). The displacement mostly affects a north-facing slope, clearly separated from area A. The dimensions of this landslide area B are 0.9 km from west to east and 2 km from north to south. This area of surface displacement was apparent throughout the available time series dataset. As area B was urbanized (the village of Makhatauri), maintenance of high coherence over long time periods appears to be possible (Usai and Klees 1999).
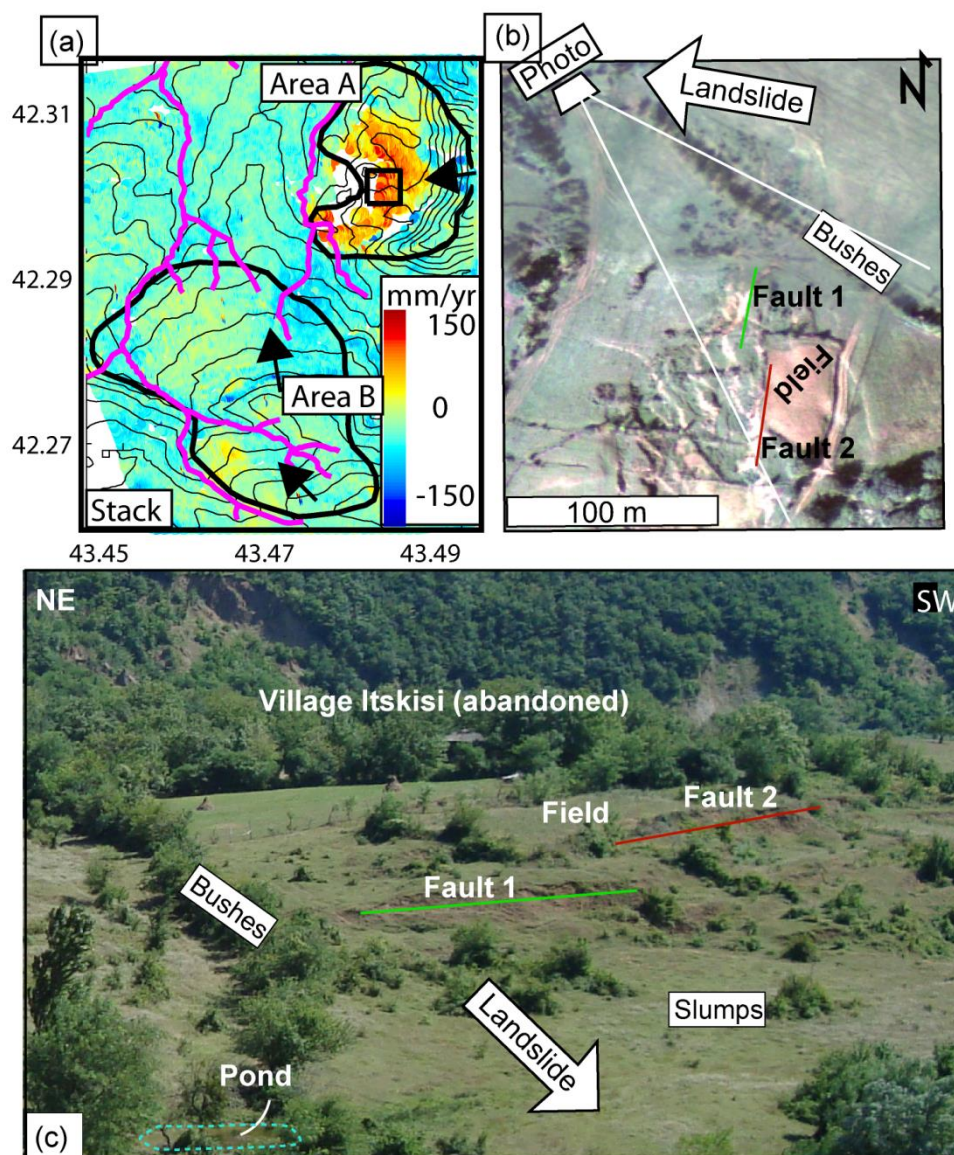
Figure 2.5. (a) The stack velocity in the LOS direction. River streams (magenta curves) and contour lines were added. The contour interval is 30 m. The arrows show the approximate directions of the landslides. The black box shows the position of the aerial photography (b) in area A. An annotated aerial photography used to map several faults and a newly developed pond identified from the aerial photography and field trip observations in August 2011 (c). The village in the background was abandoned.

The SBAS pixels covered the whole investigated area more evenly than the PS pixels. An analysis of the distribution of the pixels overlapping high-resolution aerial photography conducted using ArcGIS revealed that the PS pixels were located mostly on the roofs of man-made structures. The SBAS pixels also covered bare land, fields of land use and rural areas.

The results of the four methods, i.e., two-pass interferometry, average velocity determined from the stack of interferograms and the PS and SBAS time series, were very complimentary, as they clearly delineated the active parts of two distinct landslides (Fig. 4). The displacement was mostly positive for landslide A, i.e., clearly shows movement toward the satellite. For landslide B, the displacement was more complex: in the central part of the landslide area, the displacement was positive, but negative motion was observed on the west and east lobes of the landslide. Using only one of the approaches, we would have detected only one of the landslide-related displacements, and which displacement was detected would have depended on the method used. These results are plausible given the selection of pixels and detection thresholds used, as further discussed in the following section.
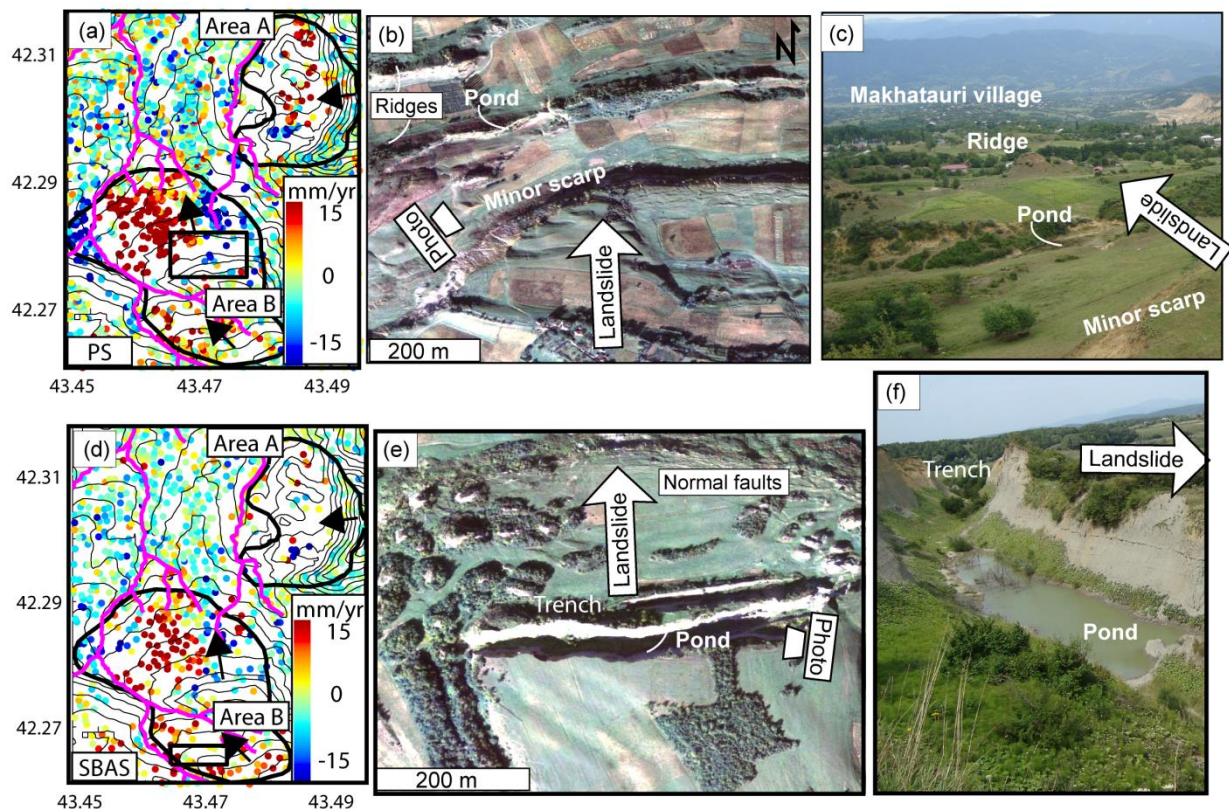
Figure 2.6. (a) The average velocity in the LOS direction from PS. River streams (magenta curves) and contour lines were added. The contour interval is 30 m. The arrow shows the approximate direction of the sliding mass. The black box shows the position of the aerial photography (b) in area B. (b) Features such as a minor scarp, ridges and a pond are visible in the aerial photography (b) and also appear in the photography taken during the field trip (c). (d) The average velocity in the LOS direction from SBAS. The black box shows the position of

the aerial photography (e). The trench is visible in the aerial photography and in photographs (f) taken during the field trip in August 2011.

2.4. Discussion

This is the first InSAR study of landslides in Georgia that has relied on a SAR dataset for a poorly monitored region. We emphasize that all of the results presented were calculated from radar measures of displacement, with only one component in the radar LOS direction. Therefore, extraction of the true horizontal and vertical displacement rates was not possible. ALOS PALSAR ascending data were available and were found to be suitable for this region only. Therefore, it is a challenge to determine the direction in which the ground moved, given that there is no ground truth or better InSAR data coverage. In this study, we therefore assumed, for the sake of simplicity, that the main movement followed the slope direction. We have also investigated several other regions in Georgia and have found that the SAR data archives are, in general, very poor in comparison to those in other countries.

Our InSAR analysis of an area 4.16 km wide and 6.85 km long in Central Georgia has revealed two areas in which surface deformation has occurred. Motion is visible in area A using the two-pass InSAR method (Fig. 4 (a)), whereas motion in area B is observed only in the results obtained using the InSAR time series approaches (Figs. 4 (b, c)). The two landslides have either different displacement velocities or different sliding directions or both. Low-velocity displacement can best be monitored using a long time interval between acquisitions (Usai 1997; Usai and Klees 1998). For the same time and the same data, displacement of one order of velocity higher may not be detectable due to decorrelation. The PS and SBAS techniques are proven to be best-suited for detection of slow movements (several mm per year), while two-pass interferometry is sensitive to more rapid displacements (several cm per year), albeit at the cost of atmospheric signal delay artifacts.

Decorrelation of the pixels used in the different processing methods will determine the success or failure of each method. Applying different InSAR processing algorithms, as we have in this study, is particularly important for landslide research, in which displacement rates and decorrelation effects may vary significantly over time and space.

The PS method focuses mainly on separate targets that have high reflectivity and are stable over the time periods between image acquisitions, while two-pass interferometry shows displacements of areas without an emphasis on

individual targets. One reason that the PS and SBAS methods choose many points inside area B (Figs. 6 (a), (d)) is that this landslide occurred in an area that contains man-made structures, such as houses. There are only a few points within the limits of landslide A in the PS results, due to the lack of coherence and the difficulty of detecting relatively large displacement rates (Colesanti and Wasowski 2006).

We should note that other processing procedures, such as Squee SAR TM (Lagios et al. 2013), WabInSAR (Shirzaei 2012) and Quasi-PS (Perissin and Wang 2011) may yield different results, given the different pixel selection procedures that they use. In addition, with the increasing availability of SAR data and the possibility of higher temporal sampling, the coherence might improve so that the two landslides examined in this study might be better investigated.

A comparison of our InSAR results with those from an analysis of aerial photography results shows that the displacements detected using InSAR data are located close to geological features that relate to landslide processes (Figs. 5-6). These features are main and minor scarps, ridges, various types of faults, ponds and trenche (Figs. 5-6 (b), (c) and Figs. 6 (e), (f)). The trench have most likely widened as a result of erosion (Figs. 6 (e), (f)). Whether shear or normal slip activity has occurred cannot be determined from our data. The shape of the deformation area generally reflects the topography in both landslides (Figs. 5(a), 6(a)). The slope in area A is west-facing. The direction of the slope face allows us to infer the direction of movement of the landslide, i.e., mostly westward (Fig. 5(a)). Examination of the contours in Figure 6(a) shows that the slopes in area B face mostly to the north, northwest and northeast. In this case, the radar system sensitivity is low with respect to the displacements (Colesanti and Wasowski 2006). North-south movement is difficult to detect with InSAR, because it is perpendicular to LOS direction. Nevertheless, the PS and SBAS methods may detect some movements in this case too (Perski et al. 2009). Negative displacements occur on the slopes facing northeast. Positive displacements occur on the slopes facing northwest. It follows that most likely only a small portion of the signal deformation was determined for area B.

The river and streams (Fig. 6(a)) curving around landslide body B indicate areas of increased erosion. The photographs show several places where the soil surface has moved downslope and formed cracks (Figs. 5-6).

Although the differences in the results obtained with the stacking process and the PS and SBAS methods are grounded in differences in coherence, the implications are broad: InSAR, as a tool for the detection, monitoring (Colesanti

et al. 2003b) and analysis of mass movements, requires a combination of processing strategies if the dataset is thin or if decorrelation due to effects such as those of vegetation and large displacement rates limits the success of time series analyses.

2.5. Conclusions

Two distinct landslide complexes have been detected using various InSAR analysis strategies. Our analysis showed that area A is moving at a rate of approximately 30 cm per year in the direction of the satellite LOS, based on examination of data from multiple periods that enable us to calculate a mean displacement rate per year. Movement in the landslide complex within area A is detectable using the two-pass and stacking procedures. When analyzing an InSAR time series, this landslide is undetected, as significant decorrelation occurs. Instead, another landslide complex (area B) appears. Area B has an extremely slow displacement rate, less than 3 cm per year in the LOS direction, based on our examination of twelve SAR images. The most likely displacement direction is to the north, i. e. parallel to the radar satellite orbit. Therefore, area B could only be identified using the InSAR time series methods PS and SBAS. The projected LOS displacement rates were hence different by an order of magnitude (30 cm/year for area A, 3 cm/year for area B). Based on a comparison of the results of the stacking process of the two-pass InSAR method with the results from the time series, we conclude that for the given scenario and dataset, landslide detection is more successful using multiple processing approaches that complement each other.

This study also highlights the need for regular SAR acquisition over Georgia, a country that has not been a focus of geodetic research, despite the region being highly geologically active.

These techniques have allowed us to define the boundary between the active part of the landslides and their kinematics. Identifying surface slope motion activity can therefore only be accomplished through a combination of methods. We propose that further investigation include monitoring of these landslides with ground-based measurements.

3. Landslide observation and volume estimation in central Georgia based on L-band InSAR

E. Nikolaeva[1], T.R. Walter[1], M. Shirzaei[1,2], J. Zschau[1]

[1]Department 2- Physics of the Earth, Helmholtz Center Potsdam – GFZ German Research Center of Geosciences, Potsdam, Germany

[2] now at: School of Earth and Space Exploration, Arizona State University, Tempe, AZ 85287-6004

Abstract

The republic of Georgia is a mountainous and tectonically active area that is vulnerable to landslides. Because landslides are one of the most devastating natural hazards, their detection and monitoring is of great importance. In this study we report on a previously unknown landslide in central Georgia near the town of Sachkhere. We used a set of Advanced Land Observation Satellite (ALOS) Phased Array type L-band Synthetic Aperture Radar (PALSAR) data to generate displacement maps using interferometric synthetic aperture radar (InSAR). We detected a sliding zone of dimensions 2 km north–south by 0.6 km east–west that threatens four villages. We estimated surface displacement of up to ~30 cm/yr over the sliding body in the satellite line-of-sight (LOS) direction, with the largest displacement occurring after a local tectonic earthquake. We mapped the morphology of the landslide mass by aerial photography and field surveying. We found a complex set of interacting processes, including surface fracturing, shear and normal faults at both the headwall and the sides of the landslide, local landslide velocity changes, earthquake-induced velocity peaks, and loss in toe support due to mining activity. Important implications that are applicable elsewhere can be drawn from this study of coupled processes.

We used inverse dislocation modelling to find a possible dislocation plane resembling the landslide basal décollement, and we used that plane to calculate the volume of the landslide. The results suggest a décollement at ~120 m depth, dipping at ~10° sub-parallels to the surface, which is indicative of a translational-type landslide.

Keywords: landslides, InSAR, Georgia, Caucasus, inverse dislocation modelling, displacement

3.1. Introduction

3.1.1. Landslides in Georgia

Landslides and related hazards are widespread in Georgia (Nadim et al. 2006; Gracheva and Golyeva 2010) and cause substantial damage annually (van Westen et al. 2012). The steep hill slopes, active geology and conditionally wet or even subtropical climatic conditions in Georgia (van Westen et al. 2012) are important factors that contribute to the high landslide susceptibility there. Over 5700 landslides have been identified, ranging from small-scale slumps to large-scale mass wasting of entire hillsides (van Westen et al. 2012). Approximately 700 of those landslides have been identified through yearlong mapping and field work activities. A recent landslide susceptibility analysis based on geology, slope classification and land cover mapping suggested that approximately 17% of Georgia is located in high-hazard zones, and another 38% is located in moderate-hazard zones (van Westen et al. 2012). Landslide concentration is especially high and covers all scales in Adzharia, a region in south-western Georgia with a humid subtropical climate, with occurrence peaking in spring and during summer storms (Gracheva and Golyeva 2010).

Together with the steep topography and wet climate, tectonics can be a significant trigger of landslides. The Ms 7.0 earthquake on 29 April 1991, for instance, triggered numerous landslides and caused a loss of infrastructure and life (Jibson et al. 1994). Some of these landslides were known to be active already, but moving slowly. For example, the slow-moving Chordi landslide accelerated and destroyed the village of Chordi shortly after the earthquake. This case highlights the importance of monitoring slow-moving landslides that may accelerate due to unpredictable external triggers. Slow-moving landslides in Georgia in particular can accelerate abruptly, especially if extrinsic factors act as triggers (Gracheva and Golyeva 2010). However, the interplay among various triggering factors has not been thoroughly investigated.

Although geologic mapping has been performed for some of these landslides, dynamic and kinematic analyses of them have received little scientific attention. As will be shown in this work, space-based data allow analysis of displacement rates and the identification of possible detachment planes of a landslide, which, together with aerial images, provide a detailed view of unstable masses and triggering factors ranging from tectonics to man-made activity.

3.1.2.   Landslide mechanisms

The dynamics, i.e. the appearance and displacement pattern of a landslide, is primarily controlled by the geometry of the sliding planes (Cruden 1986). These planes are made up of a combination of basal décollements and laterally delimiting fractures. The décollement is usually not directly visible and is also difficult to infer from remote sensing techniques. Therefore, little is known about the geometric complexities and dynamics of active décollement planes. The laterally delimiting fractures, in turn, are visible at the surface and commonly include a headwall fault, which is the surface expression of the main detachment, en echelon sets of strike-slip and normal faults on either side with opposite senses and a compressional zone in the landslide toe that forms thrust and fold belts. The geometry of these sliding planes affects the different types of movement. Movement of a landslide can be translational, rotational, or complex (Cruden and Varnes 1996). Rotational landslides move generally downward and outward and are thought to be structurally confined by a curved basal detachment plane (Highland and Bobrowsky 2008). Translational slides move hillslope-parallel and are structurally defined by a planar slope-parallel plane (Highland and Bobrowsky 2008). Most landslides likely involve a combination of rotational and translational mechanisms. Because the network of these structures delimits the mass of a landslide, structural characterisation of a landslide is important for assessing the landslide volume. Landslides exhibit a wide range in velocity, from extremely slow ($10 mmyear^{-1}$) to extremely rapid landslides (10 m/s) (Cruden and Varnes 1996). This broad velocity range highlights a common problem in landslide monitoring: the ability to detect and explore several scales of displacement magnitude. This problem is described further in the following section.

3.1.3.   Landslide detection and displacement monitoring

Most active landslides are studied using field-based morphological, structural and kinematic analyses. Ground-based techniques are not appropriate for detecting a landslide in a broad area because of their time and financial costs. Non-intrusive remote sensing techniques have therefore become widely used for the detection and mapping of the position, size and shape of landslides (Cardenal et al. 2001; Guzzetti et al. 2012) and potentially unstable slopes (Colesanti and Wasowski 2006; Ouimet 2010). Remote sensing techniques have specifically contributed to define states of activity, to monitor landslides, to

improve hazard analysis and to allow implementation in early warning systems (Canuti et al. 2007). Remote sensing methods include aerial photographs, multispectral optical images (Qi et al. 2010), differential Digital Elevation Models (DEMs) (Casson et al. 2005), interferometric analysis of radar images (Riedel and Walther 2008) and lidar data (Schulz 2004; Jaboyedoff et al. 2010) and others.

The most commonly used method for landslide detection is the visual interpretation of optical images (Tofani et al. 2013). Change detection techniques (Nichol and Wong 2005) and classification with semi-automated object-oriented methods (Martha et al. 2010) in optical imagery allow for landslide mapping. Together with detection, these methods allow monitoring and reconstruction of year-long time series. For instance, rapid and large morphometric changes can be quantified using change detection methods applied to high-resolution optical data (Nichol and Wong 2005). The combination of these methods is also used to improve landslide inventory maps (Guzzetti et al. 2012).

Interferometric synthetic aperture radar (InSAR) techniques allow mapping of ground movement that occurs between two acquisition times (Hanssen 2001). InSAR techniques are increasing in popularity for landslide applications (Colesanti and Wasowski 2006; Riedel and Walther 2008; Tofani et al. 2013) as they are low-cost, almost globally applicable, high-resolution and independent of day or night. The traditional two pass differencial InSAR method allows the detection and monitoring of slow (several cm per year) landslides, following the classifications of Cruden and Varnes (1996). Persistent scatterers SAR Interferometry (PS-InSAR) and Small BAseline Subset (SBAS) techniques allow analysis of the temporal and spatial evolution of extremely slow landslides (several mm per year) (Colesanti et al. 2003a; Hilley et al. 2004; Guzzetti et al. 2009). Combinations of different InSAR techniques are useful to detect and investigate different rates of landslides (García-Davalillo et al. 2013).

Each of these techniques has its advantages and disadvantages. Combining optical and radar techniques creates good conditions for the study of landslides (Strozzi et al. 2013). In this work, we exploit aerial optical, satellite spectral and, foremost, InSAR data to analyse the dynamics and changes of a landslide.

3.2. Study area

We concentrate our study on a site located in the central western part of Georgia (42.30° N, 43.48° E) because of the known landslide potential, slope angle and field access there. We use a specific constellation to investigate the effect of extrinsic forcing (Fig. 3.1). Geologically, the region belongs to the Dzirula block, which is a topographic feature of the Chiatura formation (Gamkrelidze and Shengelia 2007) (Fig. 3.1). The geologic Chiatura formation was created by sedimentary deposition, with a sequence of quartz-arkosic sandstones and sands underlying an ore horizon that is overlain by siliceous sedimentary rocks to the west and shales and shaley sandstones to the east (Edilashvili et al. 1974; Leonov 1976).
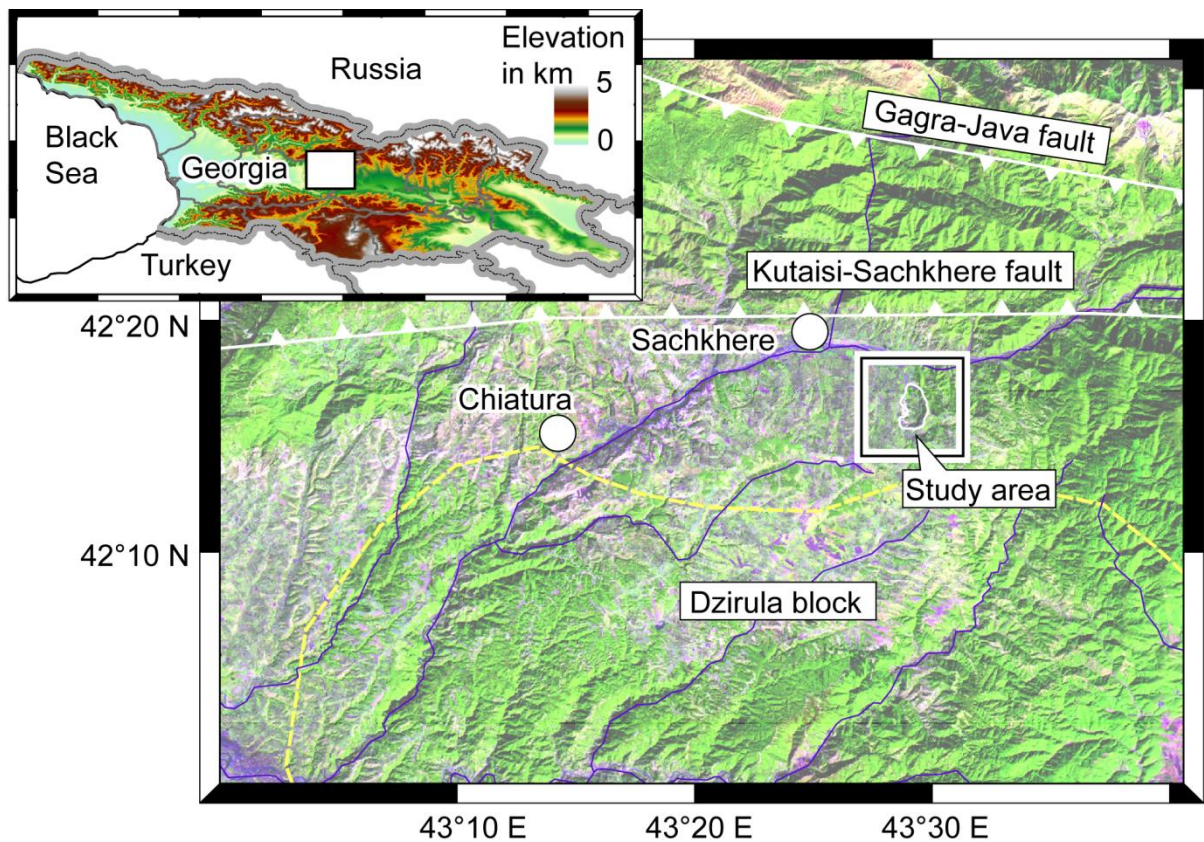
Figure 3.1. Map of central Georgia showing land cover based on Landsat TM information. The combination of bands 5, 4 and 3, represented with red, blue and green, respectively, shows vegetation in bright green colours and soil in mauve colours. The violet curves close to Sachkhere and Chiatura show the main path of the Kvirila River. The location of the Itskisi landslide is near Sachkhere (white contour). Faults indicated by white symbols are thrust faults. The faults were defined by Gamkrelidze (1978).
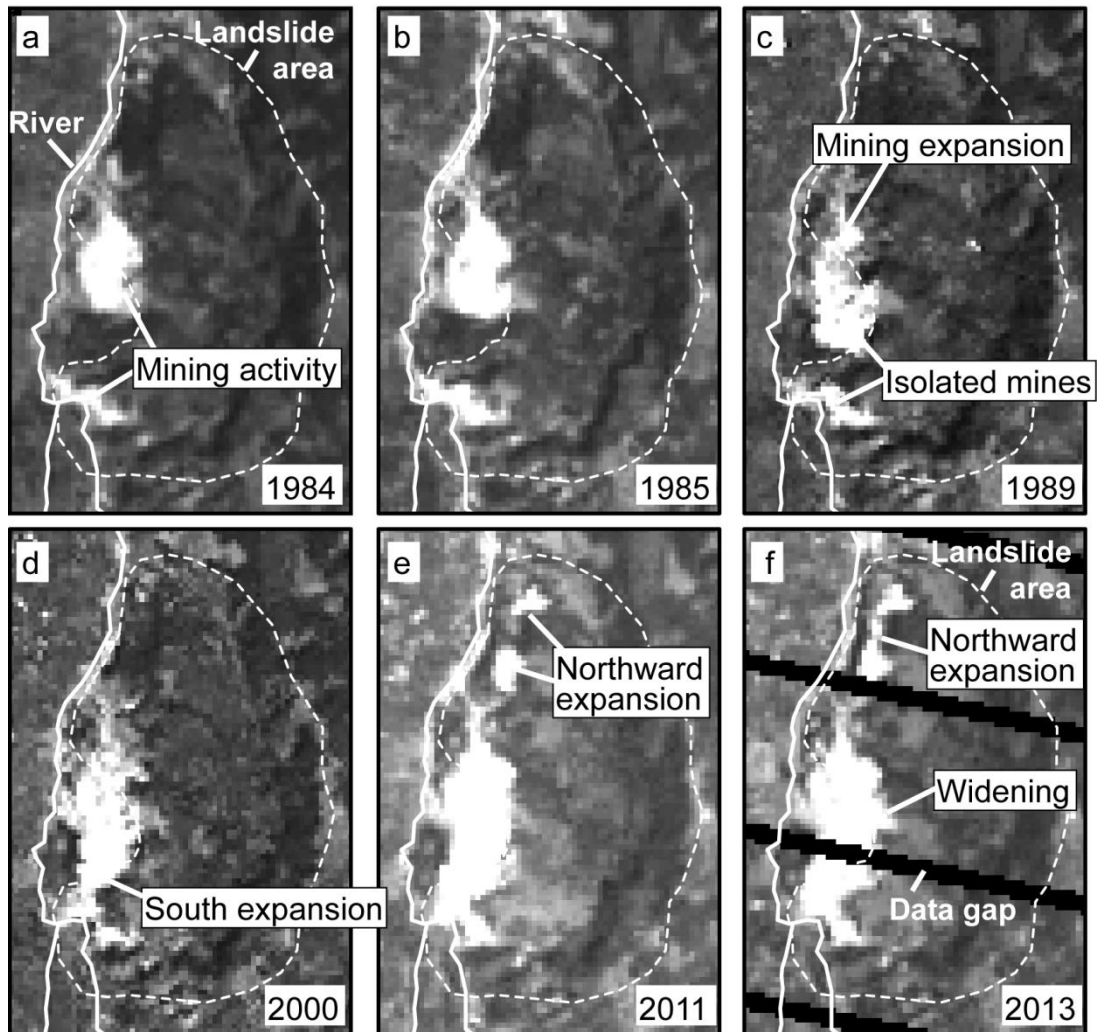
Figure 3.2. Time series of Landsat images showing the development of the mining area. The spatial resolution of the images is 30 m. These images emphasise the vegetation and the boundary between land and water. Bright colours indicate bare soil, which in this case is the mining area. Panels (d-f) show several expansions that opened over the last 20 years.

The relief profile of the study area shows a gently sloping morphology. The height varies only from 500 to 850 meters; thus the slope is moderate, with slope angles less than 20°. A significant part of the lower landslide flank is subject to mining activity (Fig. 3.2), where quartz sand is excavated. The nearby Kutaisi-Sachkhere thrust fault, located just ~5 km to the north of the landslide area (Gamkrelidze and Shengelia 2007), is thought to be active (Seismic Catalogue of Georgia, http://seismo.ge) and thus has the potential to be an unpredictable landslide trigger (Fig. 3.1). Other faults at larger distances may also dynamically trigger the landslide, similar to the 1991 Racha earthquake-

triggered landslides at over 30 km distance (Jibson et al. 1991; Jibson et al. 1994).

3.3. Data and methods

3.3.1. Data

Data analysed comprise (a) satellite radar observations, (b) optical Landsat data and aerial photographs, (c) digital elevation data and (d) field inspection. The main focus of this work is on the satellite radar observations and interferometric processing.

To generate the InSAR maps, we considered 12 the Phased Array type L-band Synthetic Aperture Radar (PALSAR) acquisitions from the Advanced Land Observing Satellite (ALOS). In standard interferometry, the quality of the SAR signals degrades due to changes in the backscattering properties of the surfaces (e.g., vegetation), which is less critical in L-band sensors (Strozzi et al. 2005). The ALOS archives of our study area contain only data acquired in ascending orbits, track 582 and frame 840, which mean that the ground is observed by the satellite only from the west. The dataset spans the period from July 2007 through June 2010. Five images are high-resolution single-polarisation (Fine Mode Single (FMS) polarisation) mode and 7 images are high-resolution, dual-polarisation (Fine Beam Double (FBD) polarisation) mode. The range resolution is 10 m for the FBS mode and 20 m for the FBD mode. The azimuth resolution is 5 meters for both modes. To avoid decorrelation associated with snow cover, we excluded scenes acquired in winter periods. The periods between master and slave images range from 46 to 138 days. The distance between two satellite positions (orbits) characterised by a spatial baseline was at most 1,885 m, which is smaller than the critical spatial baseline for ALOS (Sandwell et al. 2008).

We also tested radar data available from other satellite missions, such as ERS1/ERS2 and Envisat (C band), however, we found the interferograms to be of very low quality. We attribute this to the shorter wavelengths of these sensors compared to that of the ALOS L-band. The C-band has difficulty penetrating through vegetation; therefore, the signal may be decorrelated due to the vegetation (Wei and Sandwell 2010). The L-band penetrates the vegetation much better than the C-band does (Wei and Sandwell 2010).

Landsat images from the Global Land Cover Facility (GLCF) catalogue were used to trace the development of the mining activity. We selected cloud-free images from the 30-year catalogue. We used Landsat TM band 7, i.e., short-wave infrared (2090-2350 nm) for Landsat 4-5 (TM), as shown in Figure 3.2 (a-c, e), and Landsat 7 (ETM+), as shown in Figure 3.2 (d, f), with 30 m resolution. The spectral reflectance of dry soil or sand increases with wavelength and peaks at wavelength 2000-2200 nm (Chudnovsky and Ben-Dor 2008). Therefore, sand is highly visible in band 7. Band 7 is also sensitive to the moisture content of the soil and vegetation. Moreover, the area of interest was analysed using aerial photographs with pixel resolution ~0.6 meter that were recorded in 2007, at the beginning of our InSAR data set. We also studied geological (Edilashvili et al. 1974), land cover and topographic maps (scale 1:5000, 1972).

An ASTER DEM (resolution 30 meter) was used for morphology analysis and InSAR processing. We also tested a Shuttle Radar Topography Mission (SRTM) DEM (resolution of 1 and 3 arc-seconds), which did not change our results.

In August 2011, we visited the area of the Itskisi landslide. We validated the evidence for this landslide and mapped fractures related to the landslide in the terrain. We found newly formed cracks hidden by vegetation, mapped and measured them with handheld GPS units, and compared them to the InSAR and aerial photography database.

3.3.2.　　InSAR

The SAR interferometry (InSAR) method is the complex multiplication of two radar images of the same ground target (Hanssen 2001). Each radar image contains amplitude and phase information. The interferogram is calculated by differencing the phase component of the two coregistered radar images. The InSAR was successfully used for landslide detection and monitoring (Colesanti et al. 2003b; Colesanti and Wasowski 2006).

To start the interferometric analysis, we coregistered all SAR images to the image acquired at 4 September 2009. Thus, each pixel in all images corresponds to the same location on the ground. Raw images from the FBD mode (14 MHz) were transformed to an FBS mode spacing (28 MHz) using the ROI_PAC (Repeat Orbit Interferometry Package) software. Using DORIS (the Delft Object Oriented Interferometric Software) software (Kampes and Usai

1999), we built interferograms that contain the phase information for each acquisition. The effect of topography was calculated and removed from each interferogram using the ASTER DEM and satellite ephemeris data (Hanssen 2001). Results are based on the assumption that the ASTER DEM properly reflects the topography during differential InSAR measurements. We generated multi-look images from interferograms with a factor of 2. The multi-looking is necessary to equalise resolution in the azimuthal and in range directions. Therefore, the pixel dimensions are approximately 9 m in the azimuthal direction and approximately 7.5 m in the range direction. The interferograms were low-pass filtered using adaptive spectral filtering (Principe et al. 2004). The corresponding wrapped phase values were unwrapped using the branch-cut phase unwrapping algorithm (Goldstein and Werner 1998b) and SNAPHU, a statistical-cost network-flow algorithm (Chen and Zebker 2002). To correct for the effect of orbital error, wavelet multi-resolution analysis and robust regression were used (Shirzaei and Walter 2011).

Some of the limitations of the InSAR method are related to geometric distortion, for instance as 'layover' and 'shadow' (Chen et al. 2011). In our case, however, the slope was mostly gentle, except for sleep sections in the mining areas, where no observations were possible. Another limitation comes from the dimensionality of displacement vectors because we did not have access to both ascending and descending tracks (Delacourt et al. 2007). Having only one viewing geometry prohibits the extraction of the 3-D displacement and may affect the interpretation of the deformation field.

3.3.3. Photographic analysis

The optical data of photographs were transferred to the WGS84 reference frame and analysed in geographical information system (GIS) using ArcMap's editor functions. Only one image was available; thus the analysis concentrated on lineaments. This includes manual delineation and classification of lineaments, fractures, streams and ponds. We used the aerial photography in close comparison to the InSAR data. Specifically, fractures and morphologic expressions in the aerial photography were compared to changes in the displacement field derived from the InSAR data. This comparison allowed us to test which fractures were active and which were not. The contour map of the area was created from an ASTER DEM in ArcMap, using 3-D analyst tools. The area and perimeter of the landslide boundary were further analysed in ArcMap.

Photography taken by a geotagging camera allowed an even closer view of the selected structures and their comparison to InSAR data.

A larger view was possible due to Landsat imagery. After importing these image data to ArcGIS, we were able to visualise the growing extent of the mining activity and its effect on the displacement field.

3.3.4. Modelling

The sliding planes of a landslide play an important role in the activity of the landslide (Petley et al. 2002; Petley et al. 2005). Knowledge of the location, shape and the size of the sliding plane allows estimation of the landslide volume. To investigate the geometry of the sliding plane of the observed displacement, we applied inverse modelling techniques. Displacement maps produced from the InSAR data were used as input data. We followed previous kinematic landslide studies (Fruneau et al. 1996; Martel 2004) where models were used to describe landslide processes. These elastic models consider a flat earth and a linear elastic rheology. In our model, the main rupture plane of the landslide was simulated by a planar dislocation plane (Okada 1985). We herein considered this dislocation plane as a first-order approximation, because the model is simplified in a geometric and a physical sense. Geometrically, the models are simplified as they rely on the half space assumption and the rectangular dislocation plane, with an upper edge being parallel to the surface. Physically, the models are unrealistic as they rely on a linear elastic rheology and a dislocation along a plane. The dislocation plane we used has 8 unknowns: length, width, depth, two-dimensional position, dip and strike angles, and dip-slip dislocation components. We used the genetic algorithm to search the model and optimise the free parameters (Shirzaei and Walter 2009), choosing a wide range of possible solutions for the model parameters as a starting point. The genetic algorithm defines a cost function and initialises the genetic algorithm's parameters. We used this type of model because large landslides have structures similar to tectonic faults (Fleming and Johnson 1989). Structures found inside a landslide (Fleming and Johnson 1989) also motivated consideration of dislocation planes in translational landslide rupture models (Fruneau et al. 1996; Muller and Martel 2000). We follow these previous works by assuming that our observed displacement fields from InSAR may be simulated by planar dislocations within an isotropic elastic half-space. All InSAR deformation measurements were inverted to test the stability of the décollement

plane. Only model parameters that emerged when the genetic algorithm had stabilised, which means that the parameters had not changed for several iterations, were considered.

3.3.5.   Estimation of landslide volume

A common way to calculate the rotational landslide volume is to assume that the soil mass has the shape of an ellipsoid (Cruden and Varnes 1996; Marchesini et al. 2008). We expand on this concept by considering a more complex and realistic landslide geometry: one containing both rotational and translational components. A translational component is considered by considering an ellipsoid segment constrained by two parallel planes (Fig. 3.3). The lower plane is the decollement as inverted from our InSAR data, and the upper plane reflects the surface expression of the landslide (Fig. 3.3). There are two semi-major axes, A and B. Consider the ellipsoid segment with decollement plane *z=h*, where *h* is the depth of sliding plane. This plane is parallel to the surface plane (*XY)* located at depth *h.* The third vertical semi-major axis *C* can be calculated as follows:

$$a = A * \sqrt{(1 - (h/C)^2)} \quad (1),$$

where *a* is the axis of the ellipse formed by a section plane *z=h*. It follows from the standart ellipsoid equation for the coordinates of point (*a*, o, *-h*). Then, we are able to calculate the volume of the ellipsoid segment, which is constrained by the two dipping planes:

$$V = \int_0^h \pi * A * B * \left(1 - \frac{z^2}{C^2}\right) dz = \pi * A * B * \left(h - \frac{h^3}{3*C^2}\right) \quad (2).$$

An alternative way to evaluate the volume of a translational or rotational landslide is based on the landslide erosion rate (Hovius N., Stark, C. P. et al. 1997; Malamud et al. 2004; Larsen et al. 2010), where the predicted volume *V* of a landslide of area *S* can be approximated by the following empirical relation:

$$V = 0.05 * S^{1.3} \quad (3).$$

The parameter 0.05 was determined empirically for soil landslides (Larsen et al. 2010). An exponent in the range of 1.1-1.3 characterises a soil landslide (Edilashvili et al. 1974), similar to our case in Georgia.

From remote sensing to landslide volume estimation
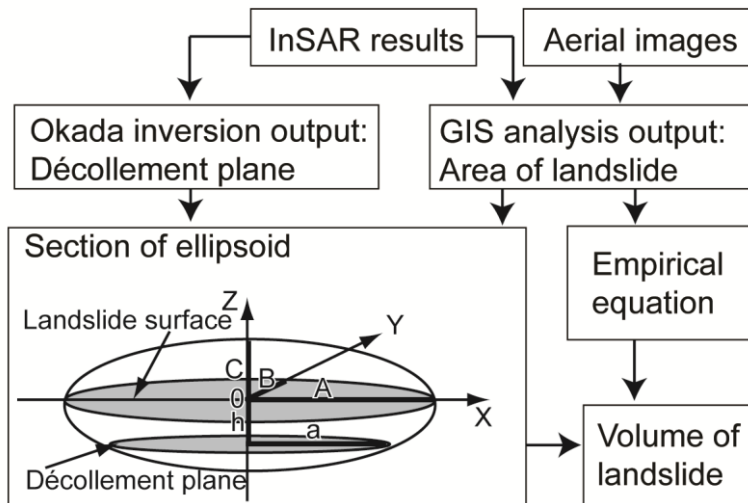
Figure 3.3. A flow chart showing data and steps taken to estimate the landslide volume and a sketch of the geometric figure that we used for the volume calculation. 'A' is the major axis of an ellipsoid in the X direction, 'B' is the major axis of an ellipsoid in the Y direction and 'C' is the major axis of an ellipsoid in the Z direction. 'h' is the distance between the plane of the landslide surface and the sliding plane. 'a' is the major axis in the X direction of the sliding plane. The volume is calculated for the area enclosed between the plane of the landslide surface and the sliding plane.

The flow chart (Fig. 3.3) shows the steps that allow evaluating landslide volumes using the above-described methods.

3.4. Results

3.4.1.   InSAR deformation field

Figure 3.4 shows the unwrapped and geocoded versions of the InSAR data set. The warm colours (positive values) indicate motion towards the satellite, while cold colours (negative values) indicate motion away from the satellite (Fig. 3.4).

We found the surface pattern of the deformation area to be roughly kidney shaped, where the major axis is approximately north-south parallel to the slope. The landslide is hence approximately 2 km long (north-south) and 0.6 km wide (east-west). A similar pattern emerges from all interferograms, which confirms the displacement occurrence. However, the amplitude of the displacement varies, occasionally even if the same duration is bracketed by the data (Fig. 3.4 a-c). This observation complicates the study because the landslide process is

found to be highly non-linear. The displacement velocity sharply increases in the interferogram from 4 September 2009 – 20 October 2009 and extends to almost the entire kidney-shaped landslide surface. The maximum difference between interferograms from 4 September 2009 - 20 October 2009 and 20 July 2009 – 4 September 2009 reaches 5 cm. We will provide more information about the possible reasons for different amplitudes in the discussion section.
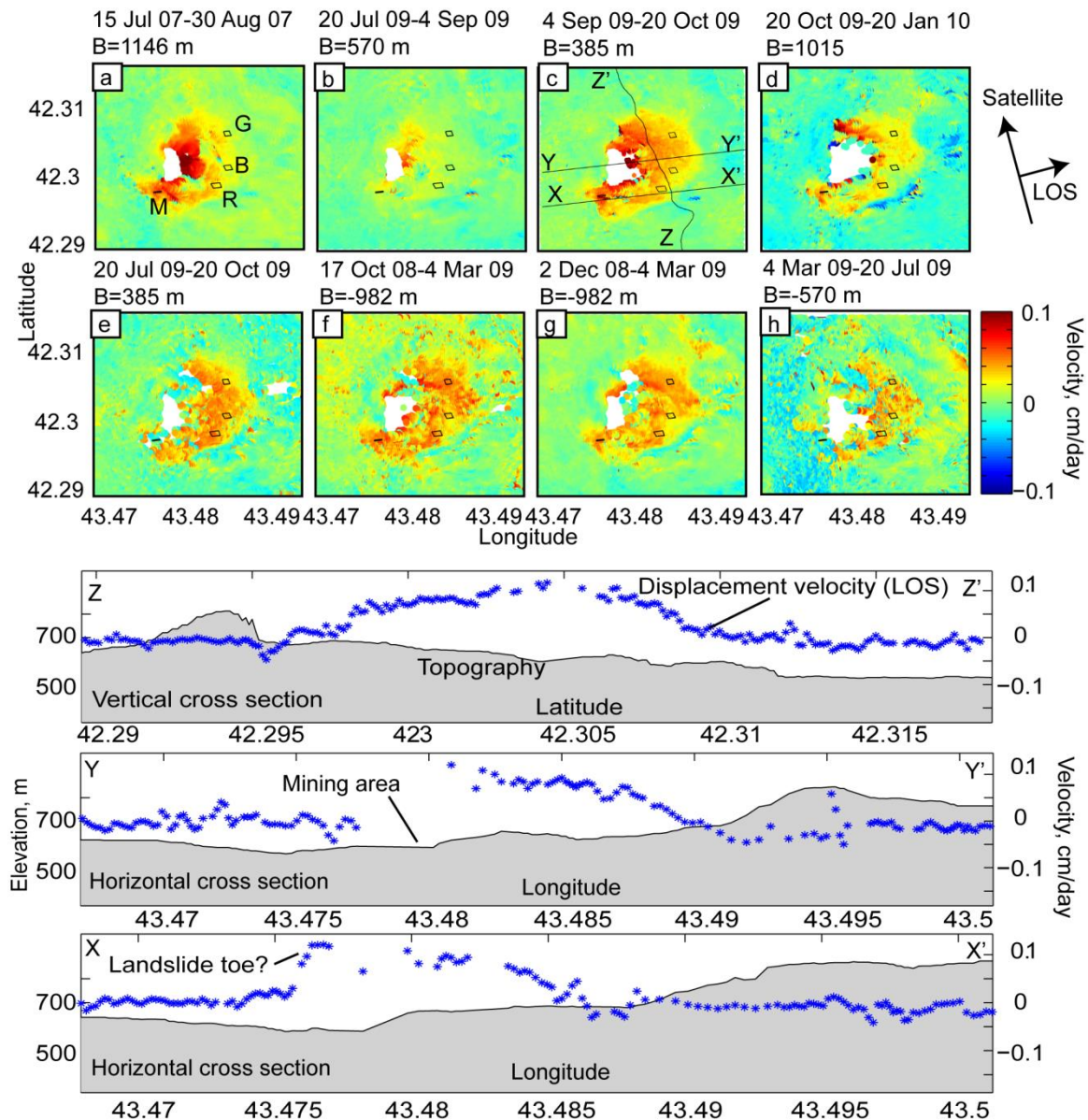
Figure 3.4. Velocity (cm/day) in the line-of-sight (LOS) direction from InSAR data. Given above each image are the two acquisition dates and the spatial baselines (B). Interferograms that are temporally or spatially decorrelated are not shown. Black lines show the profiles on plot (c), for which the topography and displacement velocities are shown below (*Z-Z', Y-Y', X-X'*). Polygons are

marked with the letters 'G', 'B', 'R' and 'M' (panel a) and present areas where average velocities were calculated for Fig. 3.9.

Three profiles taken from one of the InSAR images (Fig. 3.4 profiles *Z-Z', Y-Y', X-X'*) clearly indicate that no displacement was observed outside the landslide. The bulk of the landslide moves at similar rates, except that sharp gradients can be observed in the toe region. The gaps (Fig. 3.4 profile *Y-Y'*) indicate areas of mining activity, where no data are presented due to mining activity, steep topography or erosion.

3.4.2. Comparison of InSAR to optical images
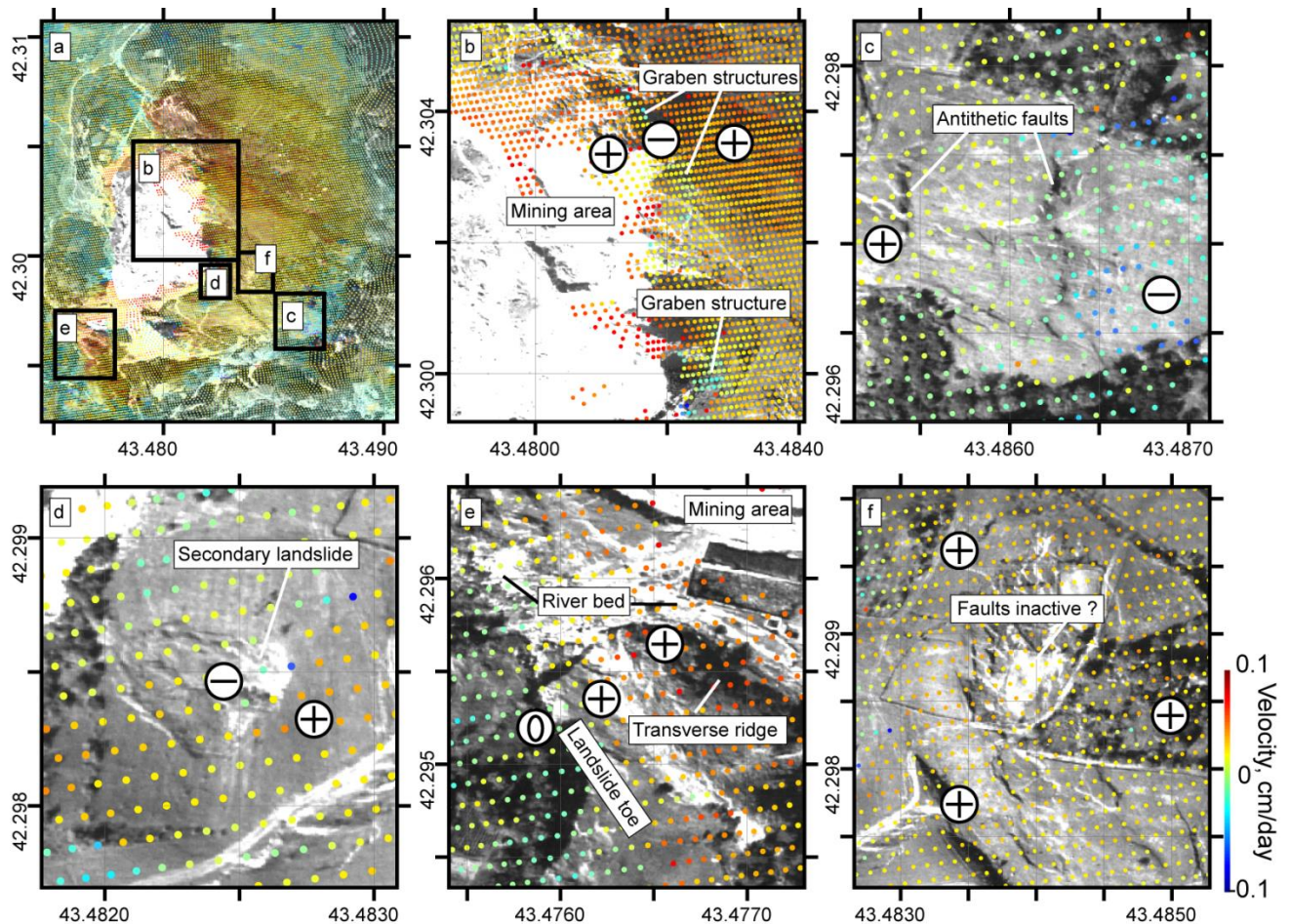
Figure 3.5. (A) Aerial photography covered by a displacement map derived from InSAR. (b-f) details of the black boxes in A, allowing a comparison between the displacement map and the morphology. Red pixels show movement towards the satellite. See text for discussion.

The surface of the landslide is hummocky and fissured. We found several local protrusions and depressions on the landslide body, which were also clear from

the profile (Fig. 3.4, profiles *Z-Z', Y-Y', X-X'*). Figure 4c presents locations of profiles (Fig. 3.4, profiles *Z-Z', Y-Y', X-X'*). We tested for correlation between the InSAR results and aerial photography (Fig. 3.5). In most cases, the displacement signals show a strong gradient within the activity zones of the landslide (Fig. 3.5b–e). Figure 3.5b shows active graben structures close to the areas of mining activity. Accordingly, these places show displacement gradients. Figure 3.5c demonstrates correlation between antithetic faults and the displacement map, best visible by the blue pixels on east side of fault. Figure 3.5d presents a secondary landslide where the scarp area has a negative displacement and the toe has a positive displacement compared to the InSAR results. The geomorphology is complex in Fig. 3.5e: the river path and the shape of topographic isolines suggest that the area was not part of the landslide. However, the displacement signal is similar to the signal on the landslide (Fig. 3.5e). This observation may suggest that the area was in fact part of the landslide. The gradient visible in the InSAR data correlates with transverse ridges, possibly associated with the landslide toe. Figure 3.5f presents an area where fault structures were observed in the field. However, the InSAR result does not show a significant displacement gradient, possibly indicating that the faults had not been active during the InSAR survey. The interferograms suggest that these and some of the fault areas are stable (Fig. 3.5a and f). It is likely that these landslide structures have either very low or no activity, or that any activity is masked by the high density of vegetation. These landslide structures are shown in both Fig. 3.5 and the survey photographs (Fig. 3.6). Because the InSAR data were available only in ascending orbits, a reconstruction of the absolute horizontal and vertical components of the displacement was not possible. We assume, however, that most of the motion is westward because the morphology displays a slope orientation to the west (Fig. 3.6a). At localised regions, significant ground movement is detected at sites with slopes facing east, thus in the opposite direction. The observation that the movement is affecting both westward- and eastward-facing slopes may lead us to speculate that the type of movement is relatively deep seated and involves both synthetic and antithetic faults (Fig. 3.6b) to form horst and graben structures. In other words, local morphologic features (Fig. 3.6c and d) and slopes have only minor influence on the moving mass, which is controlled instead by the large-scale topography and a deep-seated décollement. Due to the slow rate of the landslide, the surface activity of the sliding area is not clear in optical Landsat satellite imagery (Fig. 3.2). Investigation of high-resolution

aerial photographs, however, reveals further structural features such as folds, steps, lineaments, faults, outcrop sites and ponds (Fig. 3.7). We used these structural features to identify the type and complexity of movement for this landslide area. We created a sketch of the landslide in GIS, using aerial and InSAR results as well as field observations (Fig. 3.7). We identified partly water-filled ponds in the transition zone of the centre to the upper part of the landslide (Fig. 3.7). Although the ponds and boggy areas are morphologically well explained, they were not present on the 1972 topographic map, implying that they developed more recently. Furthermore, some houses were built in locations where ponds are located today, for instance, close to the eastern slope (latitude 42.2975^o N, longitude 43.488^o E). In the field, we identified trees or their remnants inside the ponds, which supports the idea that the ponds have appeared recently. We identified visible scarps for this region from the aerial photograph and field observations (Fig. 3.7). The major areas of debris are on the eastern slope of the landslide. Over the course of our field season, the debris flow tracks, debris fan deposits and scars evolved. Newly formed cracks hidden by vegetation were found during field surveying. The area affected by landslide processes was calculated in GIS using a polygon created based on InSAR, aerial photography and field observations (Fig. 3.7). We found that the area of the kidney-shaped landslide identified by its morphology is approximately 2.9 km^2, the perimeter of total area affected by the landslide is approximately 7.48 km, and the area having a displacement signal from InSAR is approximately 0.9 km^2.
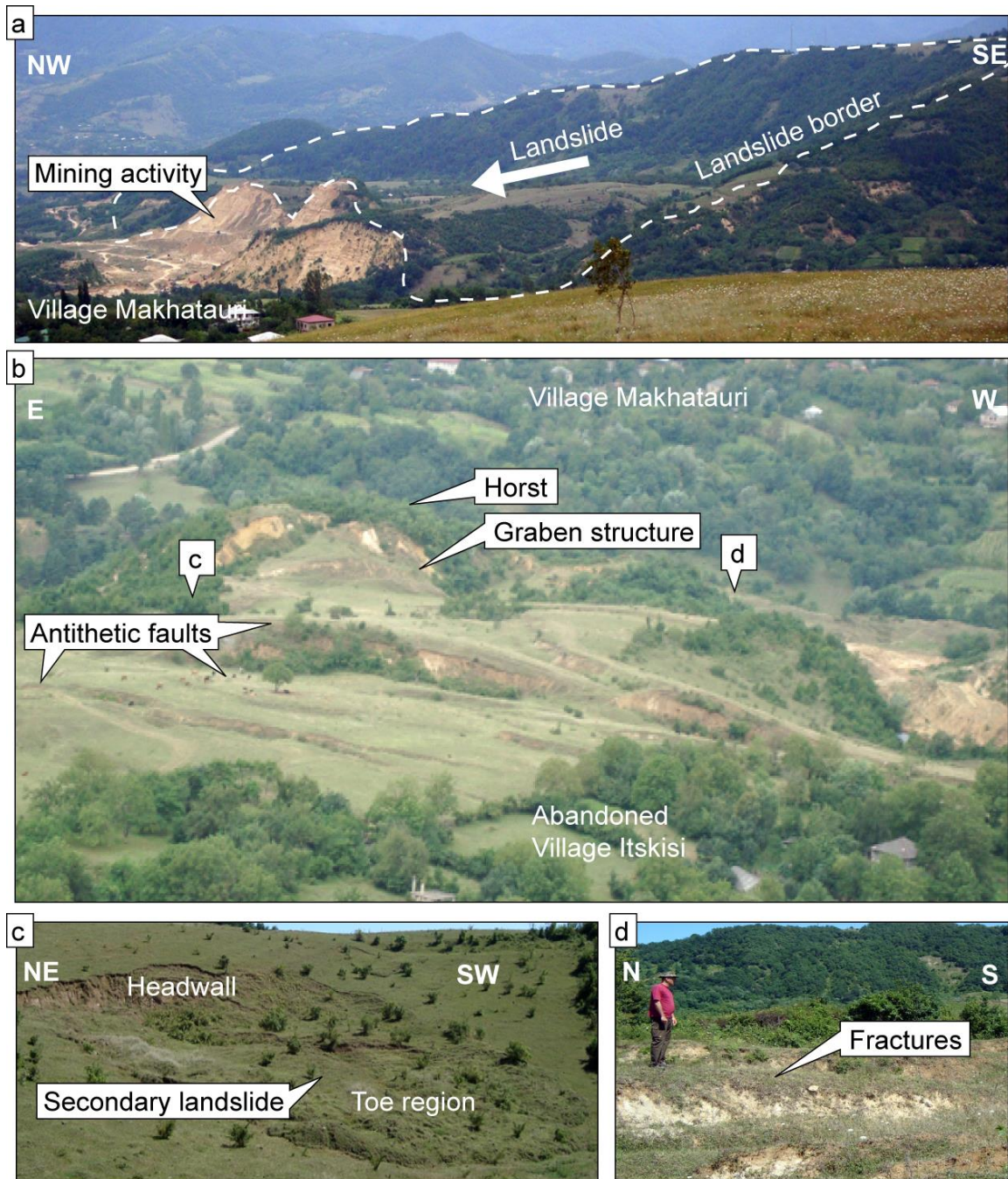
Figure 3.6. View of the landslide from the northeast (a) and from the back of the landslide, east-west (b). There are slopes cut by mining activity in image (a). The white arrow shows the direction of landslide movement. The view of the landslide from the back (b) shows landslide activity structures that are present in the aerial photography correlated with the InSAR signal in Figure 3.5. (c) and (d) show secondary landslides and fractures, respectively. Their positions are shown in image (b).
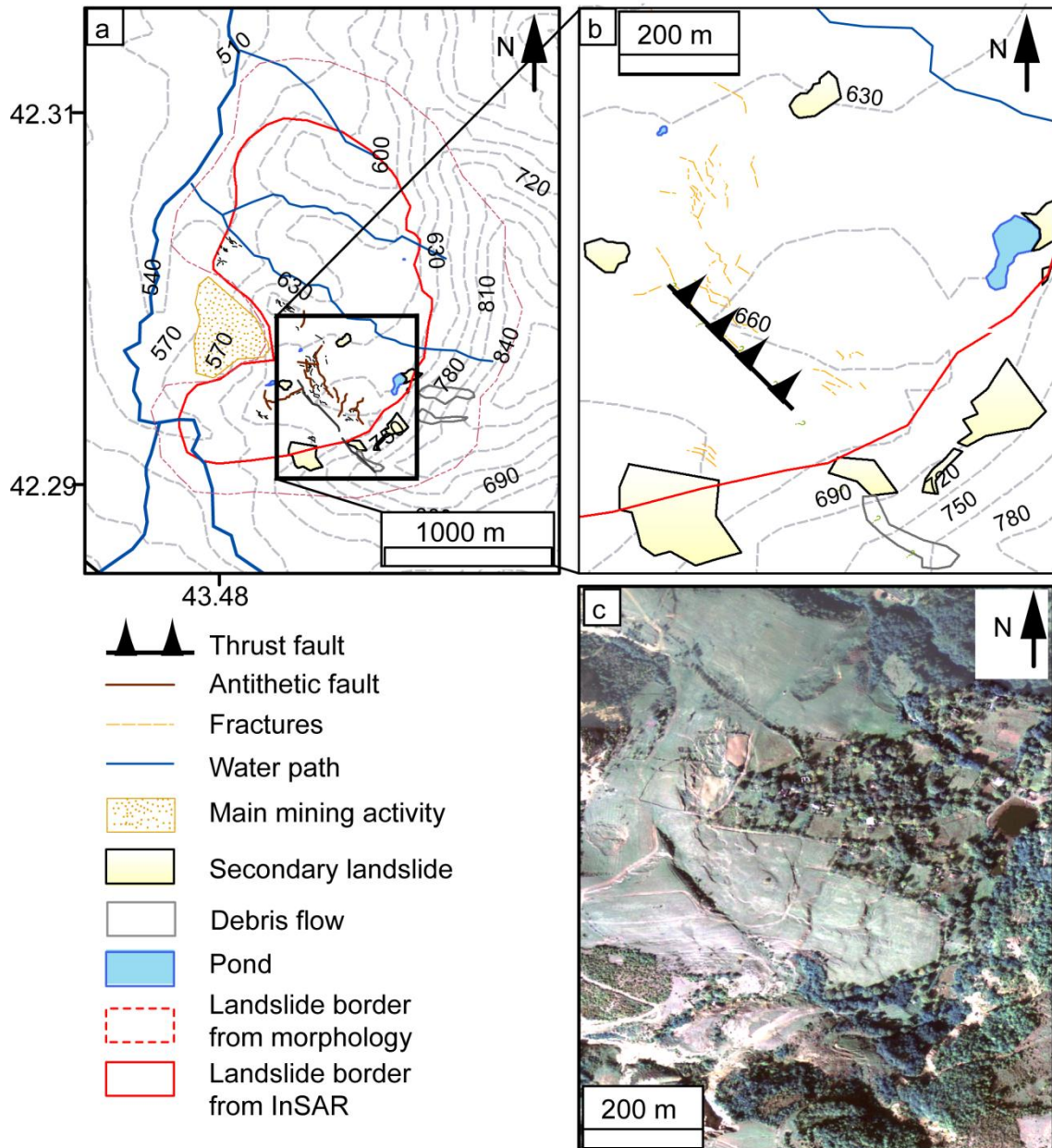
Figure 3.7. Simplified structural map of the Itskisi landslide. Contour lines are based on SRTM DEM and have 30-meter intervals. The features mapped are presented in the legend. The possible body of the landslide is within the red line (a). The red dashed line shows the landslide boundary detected from the morphology. (b) is a detail of the black box in (a). Aerial photography shows the fissured, hilly surface of the landslide (c). Structures are well aligned with the orientation of the Okada plane, as obtained from modelling of the landslide process (Fig. 3.8, Table 1, strike parameters).

3.4.3.   Modelling results

We inverted the three best interferograms with temporal baselines of 46 or 92 days. Figure 3.8 shows the observed displacements from InSAR data, model simulations of the same geometry and residuals that show the difference between those two displacement fields. In all these data sets, the optimum décollement plane is sub-horizontal and dips slightly to the northwest. The residuals are generally less than 5 cm, which means that the signal was simulated very well and the residuals approach the noise level. The highest residual is in the deposition zone of the landslide. Table 1 shows the output parameters for the model initiated with different values of input parameters. We detected a slight variation in the location and geometry of the sliding plane. For example, the dip ranges between −2 and −12 westward, the strike ranges etween 35° and 45° northeast–southwest, the dip slip ranges between −0.12 and −0.17m to the northwest and the depth ranges from 120 to 190m below the surface. As these inversions provide an indirect view on the décollement plane, we can now elaborate on the landslide volume.
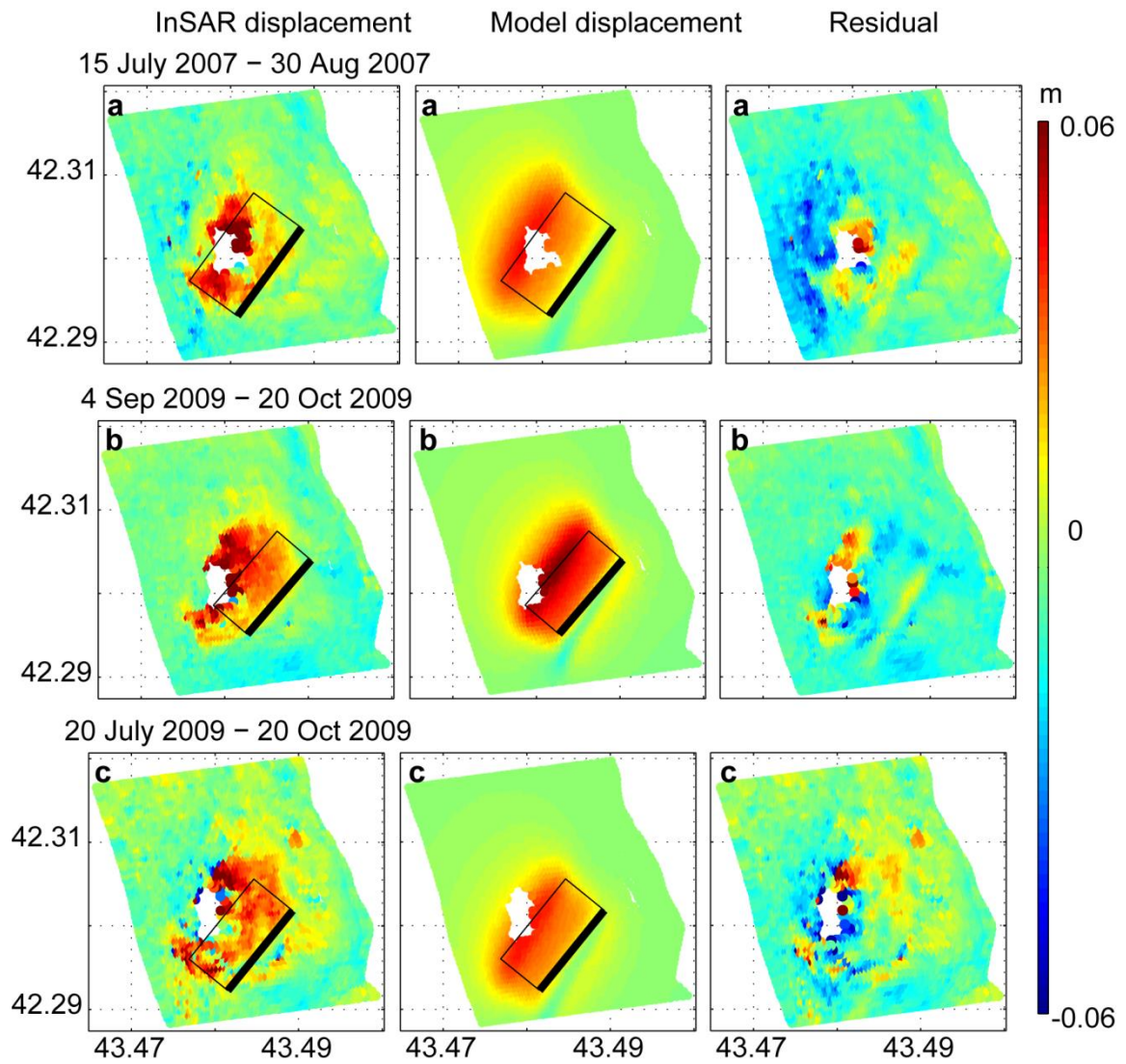
Figure 3.8. Observed quantities (left), modelled quantities (middle) and the residual (right). The mining activity was not accounted for in the modelling. The parameters of the model are given in Table 1.

case	Temporal baselines, days	Length, km	Width, km	Deep, km	Dip	Strike	Dip-slip, m
a	46	1.45	0.8	0.19	-9°	-36°	-0.134
b	46	1.3	0.6	0.12	-8.2°	-40°	-0.17
c	92	1.37	0.67	0.14	-7.4°	-39°	-0.12

Table 1. Output parameters from inversion model for different interferograms (Fig. 8 (a-c))

55

3.4.4.   Landslide volume

Using the ellipsoid segment concept, we calculated the geometrically predicted volume based on the surface affected and the location of the décollement plane. We present displacement on the surface as an ellipse with semi-major axes A and B, which have values of 1 and 0.3 km, respectively (Fig. 3.3). The axis A is found from modelling as the length parameter (average 0.65 km) and h is the modelled depth of the detachment plane (average 0.12 km). Based on these parameters and using Eq. (2), we estimated the volume of the Itskisi landslide to be 0.09 km^3. We did not include dip in our volume estimation because the slope of the target area is approximately 10, which is similar to the dip angle of the décollement as obtained from inverse modelling. Following the empirical Eq. (3) and using the affected landslide area as determined from InSAR, we obtain a landslide volume of approximately 0.046 km^3, which half the volume is estimated above. Several reasons may explain this difference. Firstly, we do not take the slope of the planes that are truncated ellipsoids into account. Secondly, the exponent 1.3 is applicable for both shallow soil-based and for deep bedrock landslides. We choose this coefficient only because we have no accurate data about the location of the bedrock. In both case, the models were simplified by the half space assumption. In other words, topography and material heterogeneity were not considered.

3.5. Discussion

 In this work, only a limited satellite radar data set was available. In Georgia this may result from a combination of political sensitivities, lack of previous scientific interest, and acquisition conflicts with other study areas.

The remaining data, however, allowed us to obtain new insights into a specific landslide case in Georgia. Eight reliable interferograms spanning over 3 years were produced to map the extent and amount of movement on the ground. Out of these, three interferograms have a noise level that makes them difficult to interprete, whereby up to 50% of the expected signal is attributed to noise. The remaining five interferograms, however, were of a high and consistent quality.

 In this work we speculate about the relationship between landslide acceleration and extrinsic processes. We note that although an earthquake occurred during the observation period, at a time coinciding with the largest landslide displacements in the InSAR data set, additional and complementary data at the landslide site would be needed to make a stronger case for a direct relationship

between these events. As long as in-site observations are not made of the Itskisi landslide or similar landslides, a clear understanding of external triggers remains elusive. The same limitation also concerns rainfall data. No accurate weather data was available to us, which is why we herein used weather models instead of in-site rain gauge observation.

The relationship of a landslide area to anthropogenic activities, here meaning mining is a critical issue. Because the Itskisi landslide has destroyed the Itskisi village and is threatening others, liability issues restrict a great deal of scientific communication between ourselves and mine operators. In addition, our own survey showed that not only one mining company but at least 17 are involved in extracting sands from the landslide toe region, which makes a control on extraction rates and volume even more difficult. Here we relied more on satellite imagery (Landsat), which clearly show the vast spread of the area of effected by mining.

We use both InSAR and optical data for the detection and kinematic analysis of a landslide in Georgia. The landslide is 0.9 km^2 in area, subject to a motion of up to 6 cm within 46 days and affects a populated region and a major mining site. Although we use radar data from a single direction (ascending satellite pass) only, the combination of InSAR displacement maps, aerial photography analysis and modelling provides information about the landslide dynamics. One of the important problems that may be encountered in the processing of radar images is the loss of coherence due to spatial or temporal factors. For this reason, we excluded some interferograms from our analysis and modelling. In the following section, we discuss the effects of extrinsic processes, such as those related to rainfall, earthquake and mining activity, on landslide dynamics.

3.5.1. Impacts

The landslide may affect surrounding infrastructure, population and river flow. landslide can dam river (Fig. 3.7), which may induce major hydrological hazards such as floods or the loss of drinking water resources. Landslide also affects erosion and can cause short-term losses of topsoil and vegetation. Landslide damming has both short- and long-term effects (Schuster and Highland, 2003). The Itskisi landslide directly affected four villages: Itskisi, Makhatauri, Savane and Irtavaza (Fig. 3.10). The village of Itskisi was located directly on the landslide and moved downslope. Houses there were damaged, and most of the

population left the village. The villages Savane and Makhatauri are separated by river at the foot of landslide. In the scenario of landslide occurrence, the landslide may block a river and reach the village Savane, which is approximately 300m away from the landslide area. The village Itavaza is located on the opposite slope of the landslide.

Understanding this type of landslide is therefore particularly important because eyewitnesses have reported increase in landslide hazards and risk over the past few decades.

3.5.2.   Factors triggering landslides

A displacement signal is detected in each interferogram shown in Figure 3.4 and is particularly strong in interferograms with short temporal baselines. Because variation in the displacement rates affects only the kidney-shaped landslide area and not the stable surroundings, we conjecture that this variation is not an artefact. The normalised velocity value suggests highly variable slip rates. The changes in the velocity may be due to variations in groundwater, which are a function of rainfall intensity or seasonal water variations such as snowmelt.

We select the average velocity at four different places on the landslide (Fig. 3.4a–h) to investigate the relationship between changes in velocity and precipitation. We compare these velocities to average monthly precipitation data (Fig. 3.9 black curve), which are based on the atmospheric general circulation model ECHAM5 (http://www.mpimet.mpg.de). The spatial resolution is roughly equivalent to 2.8 degrees in both directions, latitude and longitude (Roeckner et al., 2003). The period from June 2007 to January 2010 has a maximum precipitation value of 150 mm. The interferograms from 17 October 2008 to 4 March 2009, 2 December 2008 to 4 March 2009 and 20 October 2009 to 20 January 2010 (Fig. 3.4) cover periods with monthly precipitation below 150mm, while all other interferograms cover intervals with monthly precipitation less than 100mm. The velocity in the interferogram from 2 December 2008 to 4 March 2009 is slightly higher (0.01 cm day−1) than in the interferogram from 4 March 2009 to 20 July 2009. However, we observe that the interferograms that display highest landslide displacements do not concur with episodes of high monthly average precipitation (Fig. 3.9). These interferograms cover the time from 20 July 2009 to 20 October 2009 and 15 July 2007 to 30 August 2007. Thus, the

apparent acceleration of the landslide in September–October 2009 cannot be explained by rainfall.

Inspection of the global earthquake catalogue (CMT) shows that a magnitude Mw=6.0 earthquake on 7 September 2009 occurred at 10 km depth and a distance of only approximately 30 km from the landslide. On 18 July 2007, another earthquake occurred, this one with magnitude Ml=3.8 at 15 km depth (http://seismo.iliauni.edu.ge/) at a distance of 12 km. The observed increase of the displacement rates at these times suggests that these earthquakes may have had a triggering influence. Such a triggering influence is in agreement with work by Jibson et al. (1994), where numerous landslides were triggered following an earthquake at a distance of approximately 30 km.

These discussions are relevant given the ongoing mining activity during the period of this study. There is 68.07 Ha of mining area covered by 17 mining companies (source: www.gwp.org, licenses issued for the use of mineral resources in Georgia), as shown in Fig. 3.2 (bright areas). These images do not allow clear analysis of the landslide, but they do show the development of mining activity (Fig. 3.2, bright areas). Quartz sand extraction began in 1968 and accelerated greatly in 2007, reaching rates that continue today. This may explain why the points closest to the active mines show the highest velocities in 2007 (Fig. 3.9, margin line, year 2007).

We conclude that the landslide may have been triggered by rainfall, earthquakes and the man-made removal of the toe. Unfortunately, due to the lack of good topographic data, ground data and field information at that time, no clear relation between the earthquakes and the triggering of the landslide movements could be found.
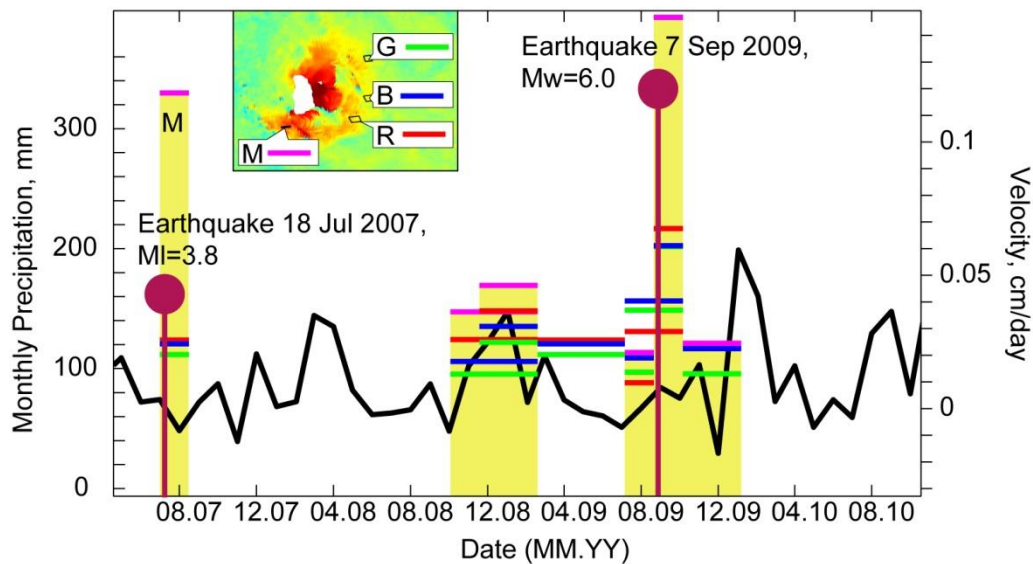
Figure 3.9. Distribution of precipitation (black curve, left scale) based on ECHAM5. The coloured lines (green-blue-red) and bar graphs (magenta) show velocities (right scale) within the area 'R', 'G', 'B', 'M' in Figure 3.4 (a).

3.5.3.   Conceptual model

Our structural mapping and analysis of InSAR data suggest that several smaller sliding blocks combine to form the larger landslide complex. We applied a model to study the internal geometry of the landslide.

Inspired by the research of Fleming and Johnson (1989), Muller and Martel (2000) and Martel (2004), we use a dislocation model to evaluate the depth of the sliding plane. The hypothesis is that the structures of large landslides are similar to tectonic faults. For instance, the seismic and geodetic observations confirmed analogous behaviour of landslide detachment planes and tectonic faults (Gomberg and Bodin, 1995). Moreover, the geometry of these two elements may also be related, as was found between adjacent ridges parallel to the San Andreas Fault in the Carizzo Plains of California and the trend of the slide-bounding strike-slip fault on the Slumgullion landslide in Colorado (Gomberg and Bodin, 1995). In our model, we had to ignore parameters that may play important roles in the development of the landslide process. We did not consider possible material heterogeneity, nor did we take into account topography or the distributions of possible driving forces and gravitation. Our model also does not show the evolution of a landslide and secondary slides and has difficulty predicting the true shape of the sliding plane. However, in the first

approximation, the model selects the potential sliding plane most susceptible to failure from an infinite number of potential surfaces. In addition, translational slides can be connected to upslope and downslope rotational slides (Fig. 3.10). The lengths of the displacement vectors remain the same at certain areas (Fig. 10, profile), and the distribution of the displacement vectors is a function of the slip-surface sliding plane (Casson et al., 2005). The equal displacement vectors in the centre zone of the landslide indicate a uniform translational landslide there (Casson et al., 2005). However, the lengths of the displacement vectors increase from east to west, which implies the presence of rotational landslide elements in the upper zone (Fig. 3.10, profile).

The complete picture of the landslide therefore consists of a planar (translational) fault at depth that curved toward the toe and headwall to form a combined rotational-translational landslide body. Secondary landslides developed and migrated, piggybacking on each other. Antithetic faults and horst and graben structures developed. The grabens formed ponds and destroyed the Itskisi village, whereas the horst structures are currently exploited by mining activity. A local girdle of subsidence surrounding the mine highlights the effects of the loss of toe support. Landslides may be triggered by mining intensification (as in 2007) or earthquakes (as in 2009). A direct link to rainfall was not found, though we note that the rainfall database was poor.

Previous studies show the efficiency of combining different remote sensing images for monitoring and characterising landslide processes (Strozzi et al., 2005; Casson et al., 2005). Using both radar and optical satellite images allows us to trace the behaviour of landslides in space and time and to evaluate an area affected by possible landslides. A conceptual model was developed based on observational data from remote sensing (Casson et al., 2005). The aim of the conceptual model is the evaluation of the volume of possible landslides for the hazard mass movement:
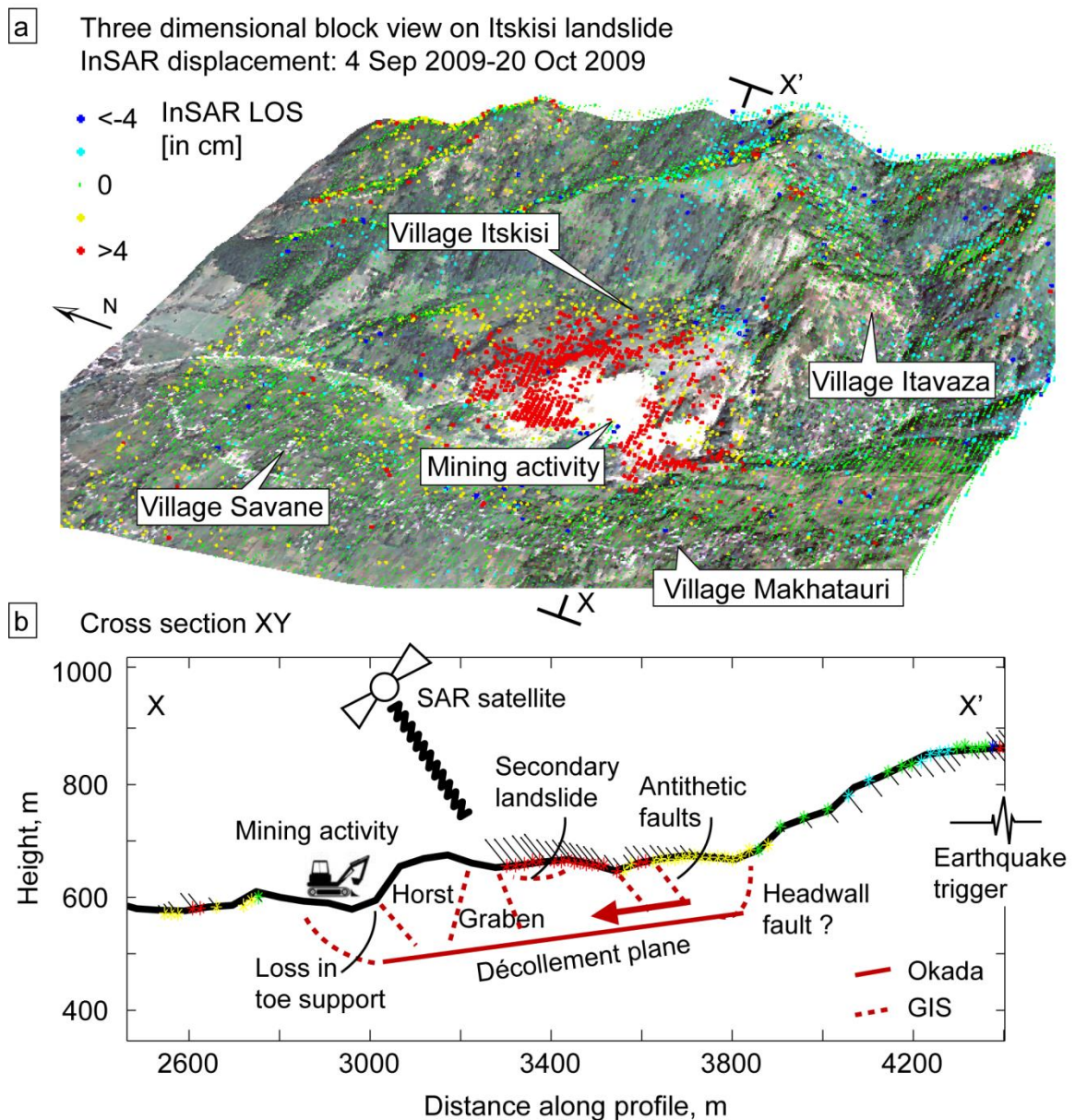
Figure 3.10. (a) Three-dimensional GIS visualisation showing InSAR-measured displacements in cm (2009 09 04 – 2009 10 20) on a digital elevation surface (ASTER, resolution 30 m) combined with an aerial photograph. The area is 3.5 km east-west by 4.8 km north-south in size. The colour scale bar indicates displacement. Four villages were affected by the landslide. (b) The profile along the region of interest runs west-east along the X-X' transect shown in (a). The colour scale for the profile points is the same as for the 3-D visualisation above. The vectors are directed to the line-of-sight. The length of the vector indicates the magnitude of the displacement, which was artificially increased by a factor of 100 for better visibility. The slip plane for the Itskisi landslide is estimated based on results from remote sensing, field observations and modelling. Our model

favours the landslide to be complex, with both a translational part (Okada model) and rotational elements (dashed red curves).

3.6. Conclusions and perspective

Landslides in the area of the Caucasus Mountains are not well monitored due to the high costs and difficult logistics of doing so. As we demonstrate, the combination of InSAR data, aerial photography analysis, Landsat imagery and other information allows us to identify and monitor a landslide in the centre part of Georgia. The displacement rate of the landslide is from 10 cm year^{-1} to 30 cm year^{-1}, covering an area of approximately 0.9 km^2. Our data suggest that the landslide movement is not stable, occasionally displaying a significant acceleration. These episodes of high landslide mobility may be associated with potential external triggering mechanisms, such as rainfall, man-made activity or a tectonic earthquake.

We characterise the landslide movement and determine displacement velocities within the landslide body. By combining this work with modelling, we are able to more precisely explore the dimensions and detachment plane geometry and further illuminate potential hazards and environmental interactions. The maximum depth of the landslide detachment plane ranges from 0.12 to 0.19 km.

Field observations show good correlation of surface fractures and the displacements obtained from InSAR data (Figs. 3.5 and 3.6). We identify a number of factors that may trigger landslides. Mining caused a loss of mass in the toe. The intensification of mining exploration locally increased the landslide velocity. In addition, the most dramatic velocity increase was found in association with a Mw=6.0 earthquake located 30 km from the landslide.

This landslide poses threats to human lives and structures that support transportation and natural resource management in four villages. The landslide or its part may be activated given the proximity (~30 km) of a possible focus of a strong earthquake (Keefer 1994; Wasowski, 2002).

This finding has important implications for hazard assessment because the location and type of landslides in Georgia apparently vary in time. The mining industry, which provides and improves infrastructure and prosperity in the region, also may contribute to triggering landslides.

Over the past 30 years, the use of remote sensing techniques in the geosciences has increased dramatically. The number of satellites with various temporal and spatial resolutions, bands and broad coverage has also increased. In this regard, there is greater opportunity to explore an event with various data sets. The probability of data being available for unexpected geological disasters is also higher. This remote sensing development plays a major role for creating a data archive for Georgia, where high hazards exist but only small numbers of observational tools are used.

The results of this study demonstrate that complex remote sensing techniques have the potential to become good tools for early warning of landslide disasters. Satellite data allow monitoring landslides in space and time. The displacement distribution obtained from InSAR data can be used in a model to characterise the geometry and spatial evolution of the landslide slip surface. Its temporal evolution can also be investigated with remote sensing data.

Our work suggests the landslide to have a decade long history, which is developing. From Landsat imagery we see that the man-made activity has significantly increased (Fig. 3.2). Our own survey and questioning of residents further support the fact that the mining activity has strongly increased in the past 8 years. One may speculate that the effect of man-made activity on landsliding may even augment more risk as unloading in the toe region continues. Moreover, as the landslide is hence further developing, also interacting processes, such as earthquake or rainfall triggering may alter with time. Therefore, close observation and further work with a more regular data acquisition are needed, allowing detection of displacement rate changes at higher detail. Also, monitoring of mining activity may also help to clarify the impact that man-made actions have on natural hazards. In this view, the Itskisi landslide may provide an excellent laboratory, where such interacting and cascading processes might be well studied.

Acknowledgements

4. InSAR observations and comparisons with the elastic dislocation model of the 7th September 2009 Racha earthquake, Georgia

E. Nikolaeva, T.R. Walter

Department 2- Physics of the Earth, Helmholtz Center Potsdam – GFZ German

Research Center of Geosciences, Potsdam, Germany

Abstract

Central Georgia is an area strongly affected by earthquake and landslide hazards. In April 1991 a major earthquake (Mw=7.0) struck the Racha region, followed by aftershocks and significant afterslip. The same region was hit by another major event (Mw=6.0) on 7th September 2009. We used the ALOS L-band InSAR data to produce an interferogram spanning the time of the second event, considering the pre-, co- and postseismic periods. We also simulated the rupture of the fault parameterized on the basis of seismic records and using an elastic dislocation model. We detected a localised uplift in the interferogram near the earthquake's epicenter whereas evidence of surface ruptures could not be found in the field along the active thrust fault, similarly to the 1991 event. The results suggest that deformation occurred in the same area where earlier damaging earthquakes were observed. We compared our modeled fault surface with the April 1991 and September 2009 Racha earthquake fault surfaces, and identify the same fault system as the origin.

4.1. Introduction

The region of Racha, Georgia, is a very active geological environment, with numerous damaging earthquakes and landslide hazards occurring during the 20th century. In 1991, a major earthquake occurred along a blind thrust fault, causing severe damage to infrastructure and triggering other hazards, such as landslides and rock falls (Jibson et al. 1994; Arefiev et al. 2006). An earlier study showed that a similar, though with a smaller magnitude, event occurred in September 2009. Landslide in the Sachkhere region showed a small, but relevant acceleration that might be associated with this event (Nikolaeva et al. 2013). In this work, we employ satellite radar measurements to detect and model surface displacement associated with the 2009 Racha earthquake. Although the deformation signal is small, and possible environmental artifacts in

the data are relevant, our model solutions suggest a rather complex fault, which is in agreement with the fault plane solutions obtained by teleseismic records, with the locations of aftershocks, and with the fault geometry as constrained for earlier ruptures, such as in the one 1991.

Interferometric synthetic aperture radar (InSAR) has been widely used to measure tectonic deformations since the first publication presented this method for the Landers earthquake (Massonnet et al. 1993). However, the focus has been on the earthquakes with magnitudes greater than 6, which produce larger deformations (Reilinger et al. 2000; Wang et al. 2004; Funning 2005). In this case, the InSAR observations often show clear signals. However, the cases of small earthquakes are less studied due to the surface displacements likely to be insignificant. Consequently, the InSAR deformation product can be mistaken by uncertainties, such as orbital errors or athmospheric contributions (Bell et al. 2012). It therefore involves additional steps to apply InSAR observations to such events to infer the parameters of a fault model that reproduces the observed deformation. Herein, we make use of data from the ALOS L-band radar satellite to detect the coseismic surface deformation associated with the moment magnitude Mw=6.0 event on the 7th September 2009 in the Racha region (the Greater Caucasus mountains).

4.2. Study area

Located at the junction between the Arabian and Eurasian plates, the Caucasus is one of the most seismically active regions in the Alpine-Himalayan collision belt. Georgia, as part of the Caucasus, is located in the central faulted segment (Fig. 1), and has experienced both historical and recent strong earthquakes.

The study area belongs to a fold and thrust mountain belt of the Greater Caucasus (Adamia et al. 2010) with shallow dipping to the North (Tan and Taymaz 2006). Consequently, the tectonics are represented mainly by vertical movements (Lilienberg 1980) and shown a general correlation with the topography (Philip et al. 1989). The geological structure resulting from the ectonic movements represents the thrust-nappe system of the Greater Caucasus. Two main tectonic units can be distinguished – one area of main ridge and one of the thrust-nappe system of the southern slopes of the Caucasus mountains. The nappe system is formed by Cretaceous to Quaternary sediments and locally maskes fault truces (Philip et al. 1989).
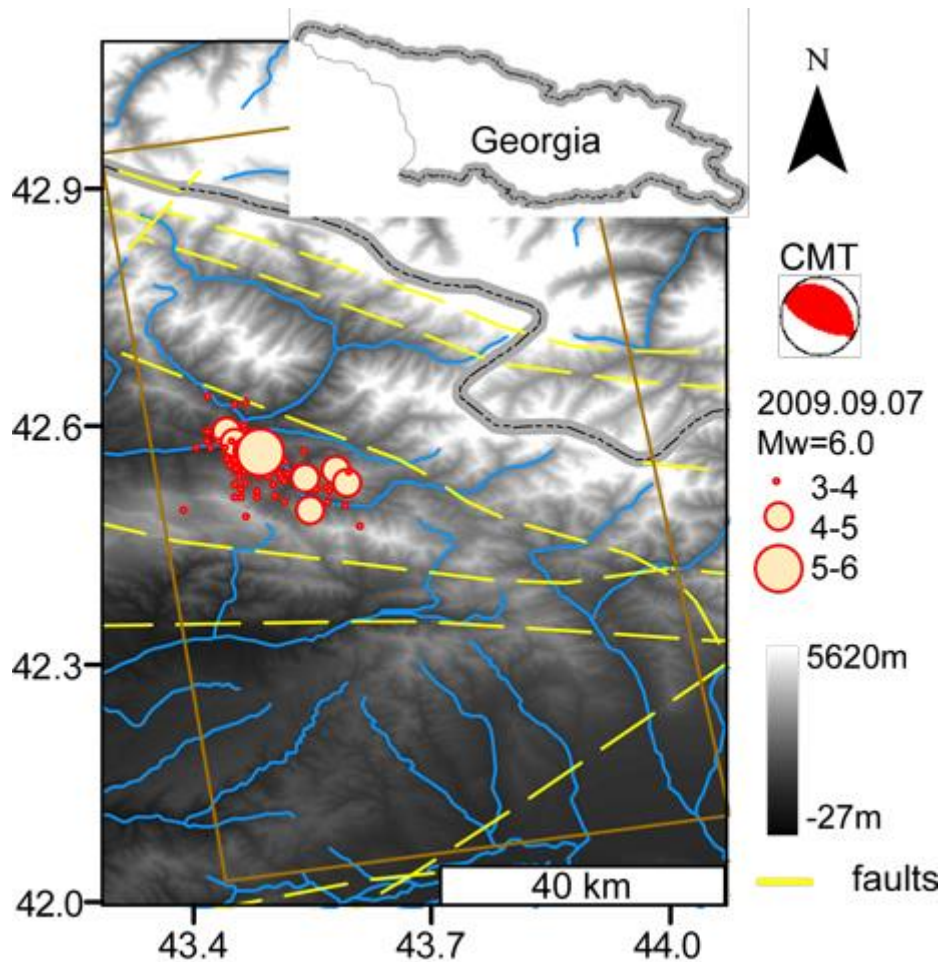
Figure 4.1. Location of the Racha 2009 Earthquake and aftershocks with magnitudes greater than 4 (www.seismo.ge). Major faults are presented by yellow dashed lines (Gamkrelidze and Shengelia 2007). The beach ball diagram is the CMT solution for the Racha 2009 earthquake. The brown frame shows the location of ALOS PALSAR images.

The seismicity of the area reflects the general tectonics of the region (Philip et al. 1989). The Caucasus represents a so-called continental collision belt between the Arabian and Eurasian plates. GPS measurements have shown that the Caucasus block moves at 13 mm/yr in an east-south direction relative to Eurasia and also has a rotational displacement component with respect to Eurasia (Reilinger et al. 2006). In addition to the seismic activity, the complicated lithological-tectonic composition of the region and with strong topographic reliefs underlines the relevance of exogenic processes, such as rainfall and erosion, accompanied by numerous landslides of different scales (Gracheva and Golyeva 2010b).

The analysis of the historical and instrumental seismological record shows that this region is of moderate seismicity. The possibility of extending the catalogue of strong events (instrumental records) until the beginning of 20th century is important for the seismic study of the region (van Westen et al. 2012).

4.3. The Racha earthquake 2009

On 7th September 2009 at 22:41 GMT or 8th September at 3:41 a.m. (local time), an earthquake with a moment magnitude Mw=6.0 occurred in northern Georgia (Global Centroid-Moment-Tensor (CMT) Project) at a depth of 13.4 km, with its epicenter at Lat=42.61, Lon=43.51. Within minutes, four aftershocks occurred with magnitude greater than 4. Other aftershocks followed, with some reaching magnitudes greater than 4 until 13th September 2009.

The main shock epicenter was located ~80 kilometers north-east of the city of Kutaisi in the Oni district of the Racha-Lechkhumi region. The mainshock was felt in Tbilisi (155 km south-east of the event), the capital of Georgia, and in the west of Georgia (Gori and Zugdidi towns). There were no reports of human losses. However, the tremors damaged at least 200 buildings, with some roads blocked by rock falls and damage to service lines (information from the Seismic Monitoring Center in Tbilisi, www. seismo.ge).

Focal mechanism solutions and the tectonic structure for the earthquake are available from the EMME (Earthquake Model of the Middle East Region, www.emme-gem.org), CMT (www.globalcmt.org) and Geophysical Survey, Russian Academy of Science (www.ceme.gsras.ru) websites.

Focal mechanism solutions were obtained from the arrival of P-waves (Fuenzalida et al. 1997). There are several minor variations in the avaliable solutions (Fuenzalida et al. 1997; Vakarchuk et al. 2013). On the basis of the available information, we gathered all the data came to follow characterization of earthquake mechanism. The type of motion was consistently defined as being thrust, roughly dipping to the northeast. Parameters from the CMT solution are strike=314°, dip=28°, slip=106°, with the moment tensor solution showing a pure thrust mechanism without a strike slip component.

4.4. InSAR data and processing steps

We combine radar images of the Racha region acquired at different time to obtain the two pass interferometric phase. Interferometric phase contains information about the difference between two independent time measurements

of the radar-to ground range (Hanssen 2001). Only the ascending track (eastward-viewing) of the ALOS satellite, L-band, are available for this area. Therefore only one line-of-sight (LOS) component of the deformation field is observable. Hence, a three dimensional velocity field cannot be extracted from this data alone.
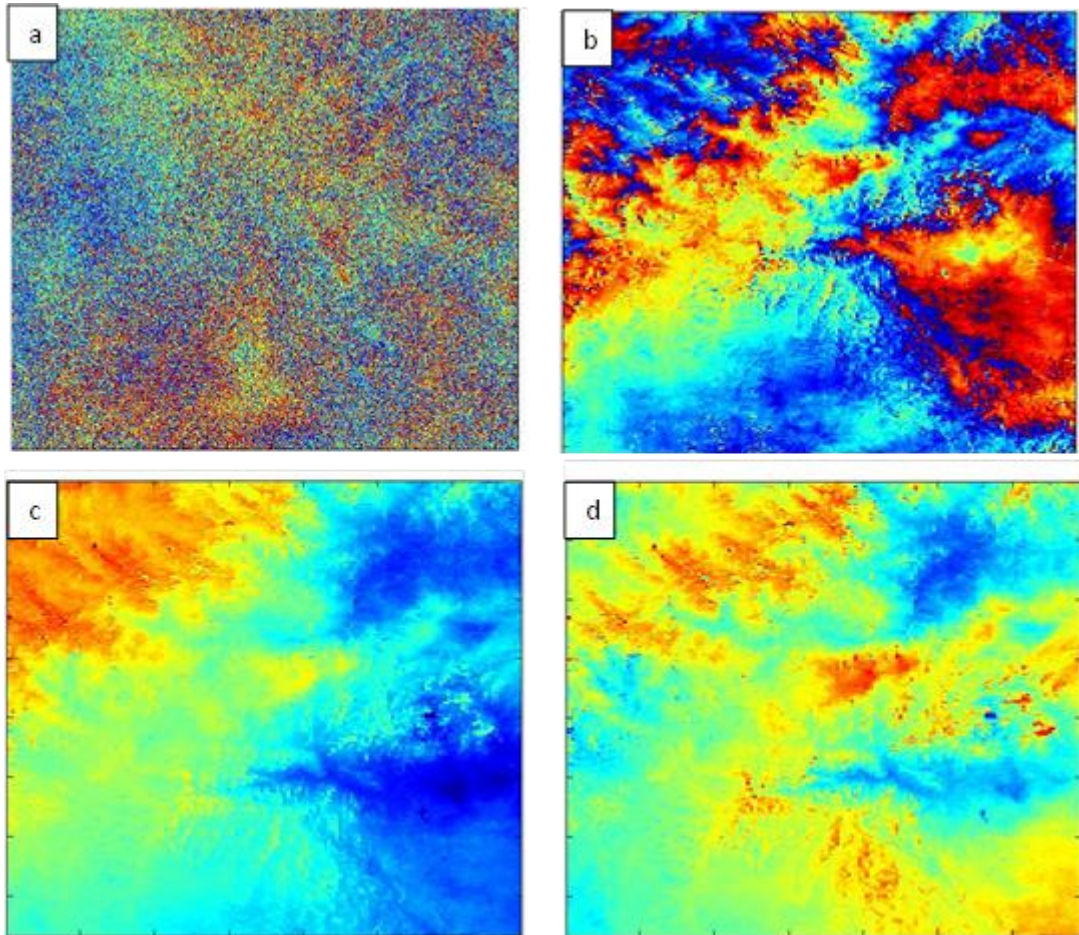
Figure 4.2. InSAR processing steps to improve the signal to noise ratio. a) Single-look interferogram, b) multilook interferogram, c) unwrapped interferogram, and d) interferograms after applying orbital corrections.

We processed eight pairs using seven SAR images. Four of the pairs covered the pre-seismic period, three pairs covered the co-seismic period, and only one covered the post-seismic. We formed single-look interferograms using whole ALOS PALSAR scenes in DORIS (Kampes and Usai 1999). The SRTM digital elevation model (DEM) was subtracted from each interferogram. Only the co-seismic pairs clearly showed a deformation, which we expect is proof of deformation associated with the earthquake.

In general, the interferogram quality was found to be rather poor. To improve the quality of these interferograms, we applied a multilooking filtering approach, so that each pixel of an interferogram represents ~200 by 200 meters square on the ground. The adaptive filter was used to smooth the speckles in the interferograms (Principe et al. 1993). We used a two-dimensional phase unwrapping algorithm to obtain unambiguous phase data. To remove the orbital contribution in the phase, we applied a wavelet multi-resolution analysis and robust regression (Shirzaei and Walter 2011) (Fig. 2(d)). Atmospheric delay was extracted using the phase-elevation ratio (Zebker et al. 1997) (Fig 3(g)). The phase-elevation correlation in the south of the image appears to be less pronounced, since the topography there is more gentle than in the north (Fig. 2). After these corrections and filtering procedures were applied, we observe some relevant signals that reflect a deformation field (Fig. 3(e-g)). Further evaluation of this deformation field was made in comparison with the dislocation model.

4.5. Modeling

We used a dislocation elastic half space model (Okada 1985) to evaluate the possible deformation from the 2009 Racha earthquake. The model calculates the deformation arising from a defined fault plane position and geometry. The model requires the following parameters: geometry of the fault plane (length and width), position of the fault in space (strike, depth, dip, coordinates of upper middle edge of fault) and the displacement components (strike slip and dip slip).

We utilized the strike and dip from the above presented average focal mechanism solution. Other parameters were calculated based on the known moment magnitude and epicenter of the earthquake. For the first approximation, we assumed that the fault size was 10 by 10 km (Donald et al. 1994). Knowing the moment magnitude (M_w), we obtained an average displacement *D =0.33* meters from formula:

$$D = \frac{M_0}{\mu A} \text{ (1)}$$

where *A* is the fault area, μ is the rigidity constant ($3*10^{11}$ dyne/cm^2) and M_0 is the seismic moment, which we extracted from the formula (Hanks and Kanamori 1979):

$$M_w = \frac{2}{3 log M_0} - 10.7 \text{ (2)}$$

For the second step, we used the InSAR observations in an inverse modelling scheme where we estimated model parameters from observed InSAR data. We included a possible geometry of fault, its depth and displacement in our estimation. The non-linear inverse problem is solved using a genetic algorithm (Shirzaei and Walter 2009).

4.6. Results

1.1.1. InSAR

All pre-seismic interferograms reveal a stable area where later an earthquake has occurred (Fig. 3 (a-d)). Three of those interferograms are spanning different time periods. Three co-seismic interferograms show a deformation signal around the fault zone area (Fig. 3 (e-g)). They are all time dependent since the second acquisition is the same for pairs. The deformation field is elongated along NW-SE and occurs in the region of the aftershocks following the 2009 event. The long axis is about 15 km, parallel to the seismogenic fault constrained earlier (Gamkrelidze and Shengelia 2007). The maximum value of deformation is around 10 centimeters in LOS. The deformation is mostly due to uplift in the region north of the alleged fault (Fig. 1). The interferogram 20090904-20091020 (yyyymmdd) is built from acquisitions 4 days before the earthquake and 42 days after (Fig. 3(f)). This interferogram is of good quality and it includes the phase changes associated with main event and aftershocks. We used this for our modeling.

Unfortunately, there is only one post-seismic interferogram (Fig. 3 (h)) of a poor. However, it shows stability for the seismicly active area.
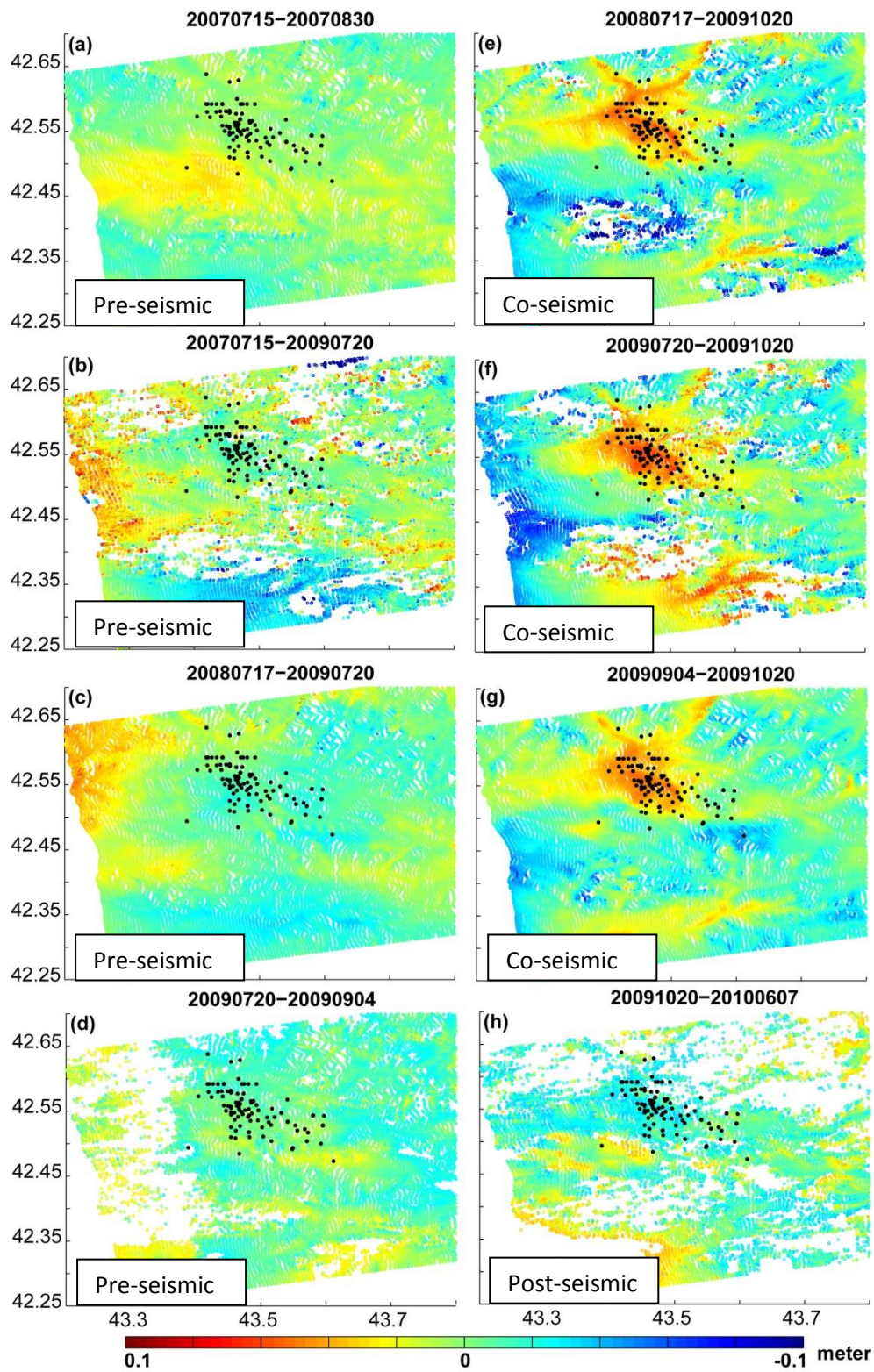
Figure 4.3. Pre-seismic, co-seismic and post-seismic deformation fields. The black dots are the epicenters of the main shock and the aftershocks with magnitudes greater than 4 (www.seismo.ge).

1.1.2. Okada model

Our initial dislocation elastic half-space model is based on the main event focal mechanism, CMT solution: strike=314^0 and dip=28^0 (Fig. 4(a)). The dip slip=0.34 m was calculated from formula (1), with the assumption that the fault is a rectangle and has the parameters length=10 km, width=10 km. The depth (10 km) and position is in the middle of the fault plane and was calculated based on knowledge of the earthquake's epicenter. The model generally reproduces the distribution of deformation, but has significant residuals when subtracted from the InSAR data (Fig. 4 (a)).
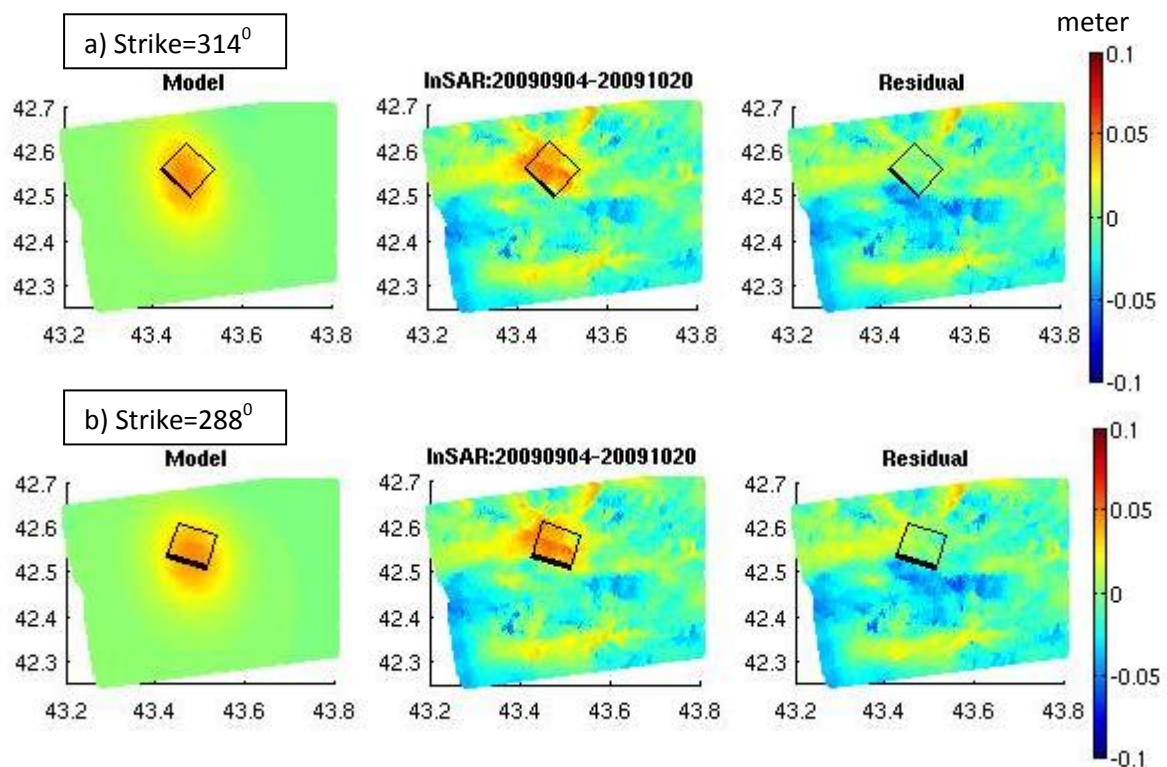
Figure 4.4. a) Model based on the CMT solution (left), InSAR interferogram (middle) and residual (right) between the observations and model. b) Same as in the previous case, but with a different strike value. The black frames show the projection of fault plane.

The shallowest edge of the fault, however, is not identical to the main orientation of the deformation from the InSAR observations in modeling case (a) (Fig. 4 (a)). We found that the modeled deformation of a fault oriented 288^0 from north clockwise better fits the deformation observed in the InSAR results. This trend is also in agreement with the 1991 Racha earthquake, the same fault ruptured,

either directly at or very close to the current earthquake rupture zone, as will be further discussed below.

4.7. Discussion

Using satellite radar interferometry, we investigated the displacement associated with the 2009 Racha earthquake. We assessed the ALOS radar data catalogue and processed data that covered the earthquake area and period surrounding.

We used inverse modeling to check our hypothesis about a shallow fault. We inverted using only the InSAR data and assumed a fixed potential mechanism suggested by the CMT focal mechanism solution. Repeated source optimizations however, failed to result in consistent source parameters meaning that the results are unstable. To understand the mechanism of the fault, we had to consider the rupture geometry within the context of previous earthquakes. For this reason, we will now briefly review the 1991 Racha earthquake, and the associated post-seismic deformation.

The 1991 Racha earthquake (Mw=6.9) was the strongest instrumentally recorded event in the Caucasus region (Fuenzalida et al. 1997). The Harvard CMT solution presented a double-couple focal mechanism equivalent to a pure thrust fault (Fuenzalida et al. 1997). The main parameters of the main shock and the largest aftershock (Mw>5.5) are given in Table 1. The aftershock distributions allowed two main branches, to be distinguished one trending $N310^0$ and the other $N105^0$.

A comparison of the epicenters from the 1991 and 2009 events reveal the same latitude and a difference of only 0.1^0 in longitude. Also, as we described before, the deformation InSAR trench fits well with a model with a strike $=288^0$ (Fig.4 (b)). This strike presents the Harvard CMT solution for the 1991 Racha earthquake (Fuenzalida et al. 1997). Therefore, the interesting question is if the 2009 earthquake occurred on exactly the same fault as the 1991 earthquake and, if yes, did the 2009 earthquake fill a seismogenic gap? Answering this question is challenging, however, because of the complexity in the rupture geometries and dynamics of these events (Fuenzalida et al. 1997; Vakarchuk et al. 2013).

Table 1. Data from Global CMT catalog

Date	Lat	Lon	Mw	Strike	Dip	Slip
29.4.1991	42.6	43.61	6.9	288/87	39/53	106/77
29.4.1991	42.38	43.75	6.1	261/62	41/50	104/78
3.5.1991	42.54	42.94	5.6	315/87	47/55	127/57
15.6.1991	42.58	43.07	6.2	138/16	49/58	44/130

The fault system for the 1991 Racha earthquake was formed by four subsources using body wave inversion (Fuenzalida et al. 1997). One subsource significantly dominates the others. Therefore, the model presents a simple single rupture pattern (Vakarchuk et al. 2013). Based on observations of separate clusters of aftershocks (Arefiev et al. 2006), the model with three complex subsources was created (Vakarchuk et al. 2013). Two subsources were presented with a thrust type of motion. The reverse type of motion was included also for one subsource. It is possible that the use of a simple model leads to instability in our case.

The hypocentral depth of the 2009 earthquake was proposed to be at 7 km instead of 15 km, according to CMT catalog (Vakarchuk et al. 2013). Also, based on InSAR data, we can assume that the fault plane may be shallower to the surface.

Although surface faulting was not observed (Arefiev et al. 2006), a large number of landslides were activated during and after the Racha 1991 earthquake (Jibson et al. 1991). The distribution of the strongest co-seismic deformations in the Racha earthquake 1991 area (Jibson et al. 1994; Arefiev et al. 2006) has a similar location to the observed InSAR co-seismic deformations associated with the Racha 2009 earthquake.

Limitations of the herein discussed results mainly may come from the quality and quantity of the InSAR data. Only one viewing component was available, and a small amount of radar data has been archived by the space agency. However, despite this, the presented InSAR results allow to develop a general concept about the displacement occurrence and are the only geodetic source available for the studied event.

4.8. Conclusion

Central Georgia repeatedly suffers from earthquakes and landslides. Here, we investigate the recent 2009 Racha earthquake. We investigated ALOS satellite

radar images, acquired in ascending mode for the period before, during and after the earthquake. We generated two-pass interferograms and after filtering could identify a significant signal that might reflect the co-seismic displacement field. Through inversion modeling we could locate the geodetic source, and model the displacement signal. Results suggest that the Mw 6.0 Racha 2009 earthquake allegedly occurred on the same fault as the Mw7.0 1991 event.

Our research demonstrates the good possibility of InSAR L-band to observe deformation arising from small tectonic events and provide new insights into the tectonic processes of the Caucasus based on radar remote sensing data. Also, InSAR data has the potential to allow us to learn more about the rupture process of earthquakes in the years after.

The main deformations were rock avalanches and landslides for both earthquakes. Thereby, the mapping of the deformation zone after an earthquake leads to resolving the distribution density of landslides in the Racha area.

If additional descending and high quality co-seismic InSAR data existed, we would have been able better determine the focal mechanism, and constrain it in three dimension.

4.9. Outlook

We are going to develop inverse modeling for InSAR data and constrain complex fault systems which were described above (Fuenzalida et al. 1997; Vakarchuk et al. 2013).

5. Conclusions

This work set out to examine the occurrence of landslides in central Georgia and associated interdependencies (earthquakes, an thropogenic activities, etc.). To this aim, we have used InSAR methods and inverse modeling, and found them to be very useful tools for evaluating source parameters. Similar tools were used to define earthquake locations and to map the resulting surface deformations. Moreover, the additional avalibility of ground observations improves and clarifies the knowledge of geological processes of an earthquake and landslide related processes.

In this thesis, we used InSAR in combination with optical data to detect, map, monitor and investigate landslides in an area that has not been monitored in detail previously. Our research has shown the possibility and limitation of different radar techniques to detect and monitor landslides with different rates. Also, we estimated the velocity and undertook source modeling to invert radar interferometry results for a previously unknown landslide. The output data in the form of velocity, depth of a sliding surface and the volume involved can be used to improve landslide inventory maps and hazard evaluation for a particular investigated landslide. Our research shows the value of remote sensing for the detection and study of landslide over the Caucasus region, an area where the ground monitoring systems are quite poor.

In the following paragraphs, we summarise the conclusions of this work, covering the detection, monitoring and study of landslides using remote sensing data and inverse modeling in central Georgia. We also describe our conclusions concerning the 2009 Racha earthquake the observed deformation due to this earthquake and model.

5.1. Landslide detection and monitoring using InSAR methods

The detection and monitoring of landslides is often a difficult task due to the lack of scientific expertise, cost of instrumentation or difficult access. Some of the difficulties could be reduced by using remote sensing methods. The main advantage of remote sensing is the wide coverage and possibility to survey data in archive and follow the evolution of the process from the past to the present. The activity of a landslide can be extracted by the use of radar images, and by InSAR methods specifically.

We presented different InSAR methods to detect and monitor landslide. In particular, we showed that it is important to use a combination of different InSAR methods to study landslides within different regimes. Nevertheless, a fast landslide is not detectable by using InSAR methods. This is because the loss of coherence between acquisitions.

The product from InSAR methods is the spatial and temporal evolution of a landslides displacement and can be used to characterize the geometry of the landslide slip surface. We introduce a chart to calculate landslide volume based on InSAR output and inverse modeling. The modeling provides the location and proportions of the landslide slip surface. The volume formula for a rotational landslide was extended to a translational-rotational landslide.

We focused our study on active landslides whose displacement rates may increase due to different triggering factors, such as regional earthquakes, mining activity and rainfall. We employed all available information to determine a link between acceleration in a landslide's movement and possible reasons for this. However, a solid database for assessing meteorological forcing was not available to us.

The combination of remote sensing and other data such as ground observations and geological analysis may allow an expansion of possible analysis. However, ground data collection is not a trivial task for areas where there are private mining companies (as in our case of landslide study). Also, the lack of geological data does not allow us to make more realistic models for this area. However, the present work can be used as guide to detect and investigate a landslide remotely for a relatively low cost.

5.2. Deformation in Racha region due to earthquake

Ground deformation of the order of 10 cm relative to the line-of-sight was inferred from the InSAR observations associated with the 2009 Mw=6.0 Racha earthquake. This deformation is in general agreement with a simple elastic dislocation model, which was calculated based on information about the earthquake's focal mechanism solution derived from waveform data. InSAR data can clarify the presented uncertainties of the source models for the Racha region and local tectonic settings.

6.   Outlook

Although the lack of geodetic data in Georgia does not allow us to construct a more precise model for landslides and the 2009 earthquake, ongoing ground truth studies in Georgia and the present and future satellite missions (TerraSAR-X, Alos-2, Sentinel-1) should bring additional information and expand and clarify the presented concepts for landslides and earthquake. To this aim, we also tested the ability of higher resolution TerraSAR-X data applied to landslides, and compare results to those from the ALOS L-band data. The results in general agree, but the quality improves. Also, it is very important to establish a link between present and past data in order to interpret the evolution of natural processes, which requires more work in the future.

6.1. Integration of InSAR results from TerraSAR-X with ALOS (PALSAR) data for landslide area, case study from Sachkhere region, Georgia

Landslides are complex phenomena. Each zone within the landslide may have a different behavior, especially if the landslide extends several hundred meters or more. Interferometric Synthetic Aperture Radar (InSAR) is a good technique to detect deformation that covers areas of several kilometers. 2-pass interferometry, persistent scatterer interferometry (PS-InSAR) and the small baseline subset (SBAS) approaches were used in this work to study landslide behavior in more detail. In our work, we used two different types of SAR (ALOS and TerraSAR-X) imagery to identify the stability of landslide-prone areas. Interferograms from TerraSAR-X imagery may detect faster ground movements easier due to the short repeat cycle (11 days) with a higher accuracy, because of the short wavelength (3.1 cm) and the high spatial resolution (1m). L-band InSAR generates better results in vegetated areas due to the long wavelength (23.6 cm) and has a good ability to form long-term interferograms. Interferograms from descending TerraSAR-X imagery (observations are made from the east) show one part of the landslide, which moves several centimeters per month. By stacking ascending ALOS data (observations are made from the west) of a long time interval (2007-2010), we detect a different part of the same landslide moving at several millimeters per year. We observed that the combination of imagery with different wavelength and different methods, provide a wide picture of the velocity field in different parts of the landslide.
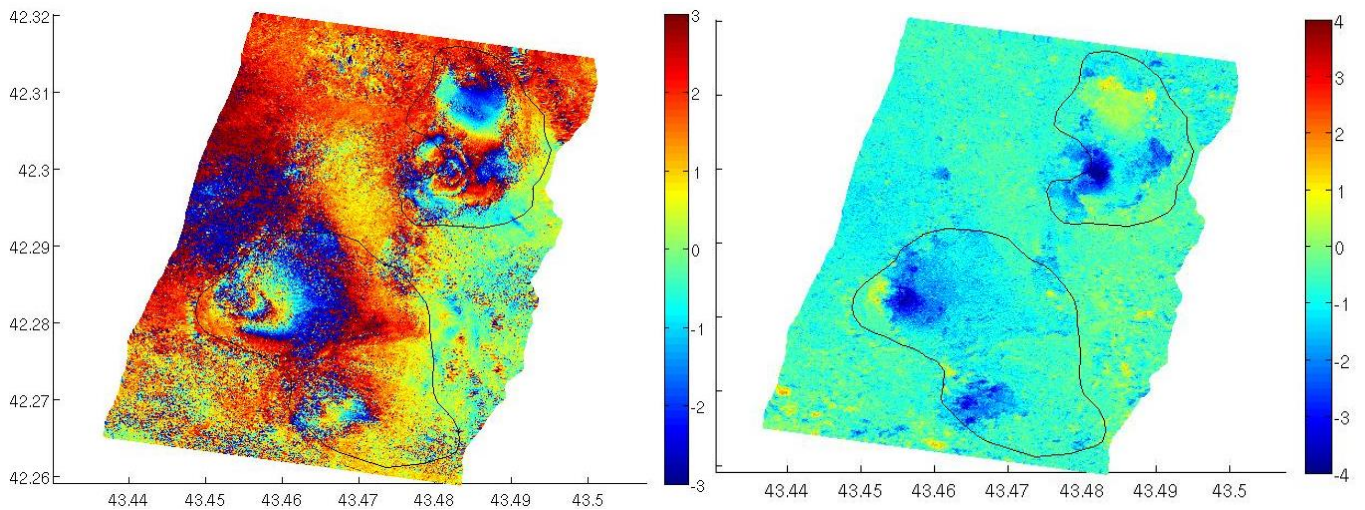
Figure 6.1. Example of TerraSAR-X wrapped interferogram (13.03.2012-11.04.2012) in the left and same unwrapped interferogram in the right.
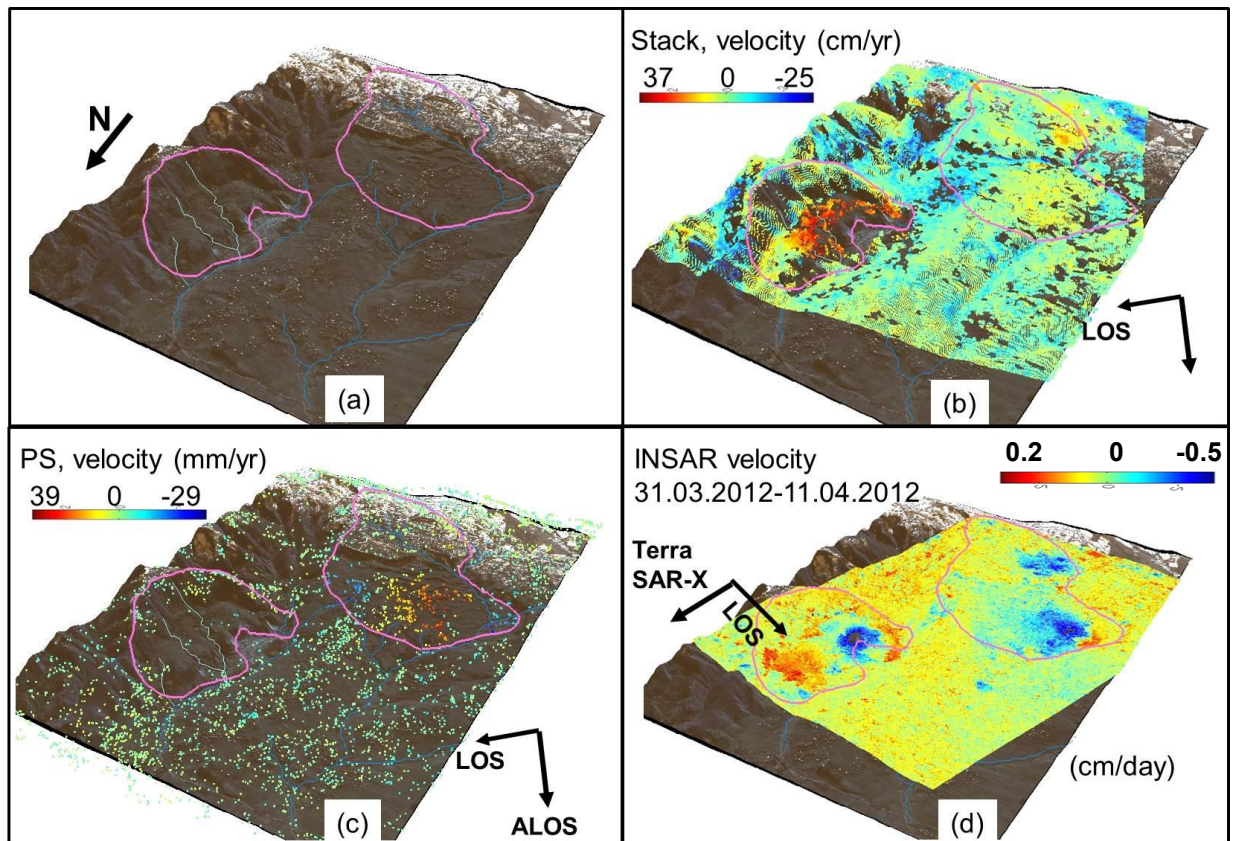
Figure 6.2. (a) Three dimensional views of the landslide area (within the margin contour) presented together with a ASTER DEM, QuckBird satellite images and polyline of the river system (blue curves). (b-c) Velocities derived from stack (b) and time series (c) InSAR L-band (ascending) images between July 2007 and June 2010. (d) TerraSAR-X data presents displacement map from the

descending track between 31 March 2012 and 4 April 2012. The highest displacement from TerraSAR-X data can be attributed to seasonal variation then when in case L-band, the average velocities covered three years were presented.

Bibliography

Adamia S, Alania V, Chabukiani A, et al. (2010) Evolution of the Late Cenozoic basins of Georgia (SW Caucasus): a review. Geol Soc London, Spec Publ 340:239–259. doi: 10.1144/SP340.11

Arefiev SS, Rogozhin EA, Bykova V V., Dorbath C (2006) Deep structure of the Racha earthquake source zone from seismic tomography data. Izv Phys Solid Earth 42:27–40. doi: 10.1134/S1069351306010034

Arnold M, Chen RS, Deichmann U, et al. (2006) Natural Disaster Hotspots Case Studies. The World Bank

Bell JW, Amelung F, Henry CD (2012) InSAR analysis of the 2008 Reno-Mogul earthquake swarm: Evidence for westward migration of Walker Lane style dextral faulting. Geophys Res Lett 39:n/a–n/a. doi: 10.1029/2012GL052795

Berardino P, Fornaro G, Lanari R, Sansosti E (2002) A new algorithm for surface deformation monitoring based on small baseline differential SAR interferograms. IEEE Trans Geosci Remote Sens 40:2375–2383. doi: 10.1109/TGRS.2002.803792

Biescas, E., Crosetto, M., Agudo, M., Monserrat, O., and Crippa B (2007) Two Radar Interferometric Approaches to Monitor Slow and Fast Land Deformation. J Surv Eng 133:66–71.

Bovenga F, Wasowski J, Nitti DO, et al. (2012) Using COSMO/SkyMed X-band and ENVISAT C-band SAR interferometry for landslides analysis. Remote Sens Environ 119:272–285. doi: 10.1016/j.rse.2011.12.013

Bulmer MH, Petley DN, Murphy W, Mantovani F (2006) Detecting slope deformation using two-pass differential interferometry: Implications for landslide studies on Earth and other planetary bodies. J Geophys Res 111:E06S16. doi: 10.1029/2005JE002593

Canuti P, Casagli N, Catani F, et al. (2007) Integration of Remote Sensing Techniques in Different Stages of Landslide Response. Prog. Landslide Sci. pp 251–260

Cardenal J, Mata E, Delgado J, et al. (2001) Close range digital photogrammetry techniques applied to landslides monitoring. Int Arch Photogramm Remote Sens Spat Inf Sci XXXVII:235–240.

Casson B, Delacourt C, Allemand P (2005) Contribution of multi-temporal remote sensing images to characterize landslide slip surface – Application to the La Clapière landslide (France). Nat Hazards Earth Syst Sci 5:425–437. doi: 10.5194/nhess-5-425-2005

Chen C, Zhang J, Lu L (2011) Identification of Layover and Shadow Regions in InSAR Image. 2011 Int. Symp. Image Data Fusion. IEEE, pp 1–4

Chen CW, Zebker HA (2001) Two-dimensional phase unwrapping with use of statistical models for cost functions in nonlinear optimization. J Opt Soc Am 18:338–351.

Chen CW, Zebker HA (2002) Phase unwrapping for large SAR interferograms: Statistical segmentation and generalized network models. IEEE Trans Geosci Remote Sens 40:1709–1719.

Chudnovsky A, Ben-Dor E (2008) Application of visible, near-infrared, and short-wave infrared (400-2500 nm) reflectance spectroscopy in quantitatively assessing settled dust in the indoor environment. Case study in dwellings and office environments. Sci Total Environ 393:198–213. doi: 10.1016/j.scitotenv.2007.11.022

Colesanti C, Ferretti A, Prati C, Rocca F (2003a) Monitoring landslides and tectonic motions with the Permanent Scatterers Technique. Eng Geol 68:3–14. doi: 10.1016/S0013-7952(02)00195-3

Colesanti C, Ferretti A, Prati C, Rocca F (2003b) Monitoring landslides and tectonic motions with the Permanent Scatterers Technique. Eng Geol 68:3–14. doi: 10.1016/S0013-7952(02)00195-3

Colesanti C, Wasowski J (2006) Investigating landslides with space-borne Synthetic Aperture Radar (SAR) interferometry. Eng Geol 88:173–199. doi: 10.1016/j.enggeo.2006.09.013

Cruden DM (1986) The geometry of slip surfaces beneath landslides: predictions from surface measurements: Discussion. Can Geotech J 23(1):94. doi: 10.1139/t86-012

Cruden DM, Varnes DJ (1996) Landslide types and processes. In: Turner AT, Schuster RL (Eds) Landslides — Investigation and Mitigation. Transp Res Board, Spec Rep 247 36–75. doi: 10.1007/BF02590167

Delacourt C, Allemand P, Berthier E, et al. (2007) Remote-sensing techniques for analysing landslide kinematics: a review. Bull la Soc Geol Fr 178:89–100. doi: 10.2113/gssgfbull.178.2.89

Donald L, Coppersmith WJ, Coppersmith KJ (1994) New Empirical Relationships among Magnitude , Rupture Length , Rupture Width , Rupture Area , and Surface Displacement. Bull Seismol Soc Am 84:974–1002.

Edilashvili VYY, Lekvinadze RD, Gogiberidze V V (1974) Effect of tectonics on manganese accumulation in Georgia. Int Geol Rev 16:37–41. doi: 10.1080/00206817409471856

Ferretti A, Prati C, Rocca F (2001) Permanent scatterers in SAR interferometry. IEEE Trans Geosci Remote Sens 39:8–20. doi: 10.1109/36.898661

Fleming RW, Johnson AM (1989) Structures associated with strike-slip faults that boundlandslide elements. Eng Geol 27:39–114. doi: 10.1016/0013-7952(89)90031-8

Fletcher K (2007) InSAR principles : guidelines for SAR interferometry processing and interpretation. ESA Publications

Fruneau B, Achache J, Delacourt C (1996) Observation and modelling of the Saint-Étienne-de-Tinée landslide using SAR interferometry. Tectonophysics 265:181–190. doi: 10.1016/S0040-1951(96)00047-9

Fuenzalida H, Rivera L, Haessler H, et al. (1997) Seismic source study of the Racha-Dzhava (Georgia) earthquake from aftershocks and broad-band teleseismic body-wave records: an example of active nappe tectonics. Geophys J Int 130:29–46. doi: 10.1111/j.1365-246X.1997.tb00985.x

Funning GJ (2005) Surface displacements and source parameters of the 2003 Bam (Iran) earthquake from Envisat advanced synthetic aperture radar imagery. J Geophys Res 110:B09406. doi: 10.1029/2004JB003338

Furuya M (2010) SAR Interferometry. In: Gupta HK (ed) Encycl. solid earth Geophys. pp 1041–1049

Gamkrelidze I, Shengelia D (2007) Pre-Alpine Geodynamics of the caucasus, Suprasubduction Regional Metamorphism and Granitoid Magmatism. Bull Georg Natl Acad Sci 175:57–65.

García-Davalillo JC, Herrera G, Notti D, et al. (2013) DInSAR analysis of ALOS PALSAR images for the assessment of very slow landslides: the Tena Valley case study. Landslides. doi: 10.1007/s10346-012-0379-8

Goldstein RM, Werner CL (1998a) Radar interferogram filtering for geophysical applications. Geophys Res Lett 25:4035–4038. doi: 10.1029/1998GL900033

Goldstein RM, Zebker HA, Werner CL (1988) Satellite radar interferometry: Two-dimensional phase unwrapping. Radio Sci 23:713–720. doi: 10.1029/RS023i004p00713

Goldstein RMM, Werner CLL (1998b) Radar interferogram filtering for geophysical applications. Geophys Res Lett 25:4035–4038. doi: 10.1029/1998GL900033

Gomberg J, Bodin P (1995) Landslide faults and tectonic faults, analogs?: The Slumgullion earthflow, Colorado. Geology 23:41–44. doi: 10.1130/0091-7613(1995)023<0041:LFATFA>2.3.CO;2

Gracheva R, Golyeva A (2010a) Landslides in mountain regions: hazards, resources and information. In: Beer T (ed) Geophys. Hazards, Int. Year Planet Earth. Springer Netherlands, Dordrecht, pp 249–260

Gracheva R, Golyeva A (2010b) Geophysical Hazards. Media. doi: 10.1007/978-90-481-3236-2

Guzzetti F, Manunta M, Ardizzone F, et al. (2009) Analysis of Ground Deformation Detected Using the SBAS-DInSAR Technique in Umbria, Central Italy. Pure Appl Geophys 166:1425–1459. doi: 10.1007/s00024-009-0491-4

Guzzetti F, Mondini AC, Cardinali M, et al. (2012) Landslide inventory maps: New tools for an old problem. Earth-Science Rev 112:42–66. doi: 10.1016/j.earscirev.2012.02.001

Hanks TC, Kanamori H (1979) A moment magnitude scale. J Geophys Res 84:2348. doi: 10.1029/JB084iB05p02348

Hanssen RF (2001) Radar Interferometry: Data Interpretation and Error Analysis. 328.

Highland LM, Bobrowsky P (2008) The Landslide Handbook — A Guide to Understanding Landslides. Landslides 129.

Hilley GE, Bürgmann R, Ferretti A, et al. (2004) Dynamics of slow-moving landslides from permanent scatterer analysis. Science 304:1952–5. doi: 10.1126/science.1098821

Hooper A (2004) A new method for measuring deformation on volcanoes and other natural terrains using InSAR persistent scatterers. Geophys Res Lett 31:1–5. doi: 10.1029/2004GL021737

Hooper A (2009) StaMPS / MTI Manual.

Hooper A, Segall P, Zebker H (2007) Persistent scatterer interferometric synthetic aperture radar for crustal deformation analysis, with application to Volcán Alcedo, Galápagos. J Geophys Res 112:1–21. doi: 10.1029/2006JB004763

Hovius N., Stark, C. P. APA, Hovius N, Stark CP, Allen PA (1997) Sediment flux from a mountain belt derived by landslide mapping. Geology 25:231–234. doi: 10.1130/0091-7613

Jaboyedoff M, Oppikofer T, Abellán A, et al. (2010) Use of LIDAR in landslide investigations: a review. Nat Hazards 61:5–28. doi: 10.1007/s11069-010-9634-2

Jacobsen K (2010) Comparison of ASTER GDEMs with SRTM Height Models. Remote Sens. Sci. Educ. Nat. Cult. Herit.

Jibson RW, Prentice CS, Borissoff BA, et al. (1994) Some observations of landslides triggered by the 29 April 1991 Racha earthquake, Republic of Georgia. Bull Seismol Soc Am 84:963–973.

Jibson RW, Randall W, Prentice CS (1991) Ground Failure Produced by the 29 April 1991 Racha Earthquake in Soviet Georgia. US Geol Surv 10.

Kampes B, Usai S (1999) Doris: The Delft object-oriented radar interferometric software. 2nd Int Symp Oper Remote Sens Enschede Netherlands. doi: 10.1.1.46.1689

Lagios E, Sakkas V, Novali F, et al. (2013) SqueeSAR^{TM} and GPS ground deformation monitoring of Santorini Volcano (1992–2012): Tectonic implications. Tectonophysics 594:38–59. doi: 10.1016/j.tecto.2013.03.012

Larsen IJ, Montgomery DR, Korup O (2010) Landslide erosion controlled by hillslope material. Nat Geosci 3:247–251. doi: 10.1038/ngeo776

Leonov MG (1976) Fractures in the Dzirula massif (Georgia). Int Geol Rev 18:1019–1024. doi: 10.1080/00206817609471311

Malamud BD, Turcotte DL, Guzzetti F, Reichenbach P (2004) Landslide inventories and their statistical properties. Earth Surf Process Landforms 29:687–711. doi: 10.1002/esp.1064

Martel S (2004) Mechanics of landslide initiation as a shear fracture phenomenon. Mar Geol 203:319–339. doi: 10.1016/S0025-3227(03)00313-X

Martha TR, Kerle N, Jetten V, et al. (2010) Characterising spectral, spatial and morphometric properties of landslides for semi-automatic detection using object-oriented methods. Geomorphology 116:24–36. doi: 10.1016/j.geomorph.2009.10.004

Massonnet D, Feigl KL (1998) Radar interferometry and its application to changes in the Earth's surface. Rev Geophys 36:441–500. doi: 10.1029/97RG03139

Massonnet D, Rossi M, Carmona C, et al. (1993) The displacement field of the Landers earthquake mapped by radar interferometry. Nature 364:138–142. doi: 10.1038/364138a0

Muller JR, Martel SJ (2000) Numerical Models of Translational Landslide Rupture Surface Growth. Pure Appl Geophys 157:1009–1038. doi: 10.1007/s000240050015

Nadim F, Kjekstad O, Peduzzi P, et al. (2006) Global landslide and avalanche hotspots. Landslides 3:159–173. doi: 10.1007/s10346-006-0036-1

Nichol J, Wong MS (2005) Satellite remote sensing for detailed landslide inventories using change detection and image fusion. Int J Remote Sens 26:1913–1926. doi: 10.1080/01431160512331314047

Nikolaeva E, Walter TR, Shirzaei M, Zschau J (2013) Landslide dynamics and coupling revealed by L-band InSAR in central Georgia. Nat Hazards Earth Syst Sci Discuss 1:4925–4962. doi: 10.5194/nhessd-1-4925-2013

Okada Y (1985) Surface deformation due to shear and tensile faults in a half-space. Int J Rock Mech Min Sci Geomech Abstr 75:1135–1154. doi: 10.1016/0148-9062(86)90674-1

Ouimet WB (2010) Landslides associated with the May 12, 2008 Wenchuan earthquake: Implications for the erosion and tectonic evolution of the Longmen Shan. Tectonophysics 491:244–252. doi: 10.1016/j.tecto.2009.09.012

Perissin D, Wang T (2011) Time-Series InSAR Applications Over Urban Areas in China. IEEE J Sel Top Appl Earth Obs Remote Sens 4:92–100. doi: 10.1109/JSTARS.2010.2046883

Perski Z, Hanssen R, Wojcik A, Wojciechowski T (2009) InSAR analyses of terrain deformation near the Wieliczka Salt Mine, Poland. Eng Geol 106:58–67. doi: 10.1016/j.enggeo.2009.02.014

Petley DN, Bulmer MH, Murphy W (2002) Patterns of movement in rotational and translational landslides. Geology 30:719–722.

Petley DN, Mantovani F, Bulmer MH, Zannoni A (2005) The use of surface monitoring data for the interpretation of landslide movement patterns. Geomorphology 66:133–147. doi: 10.1016/j.geomorph.2004.09.011

Philip H, Cisternas A, Gvishiani A, Gorshkov A (1989) The Caucasus: an actual example of the initial stages of continental collision. Tectonophysics 161:1–21. doi: 10.1016/0040-1951(89)90297-7

Principe JC, Vries B De, Oliveira PG De, et al. (2004) The gamma-filter-a new class of adaptive IIR filters with restricted feedback. IEEE Trans Signal Process 41:3378–3393.

Principe JC, De Vries B, De Oliveira PG (1993) The gamma-filter-a new class of adaptive IIR filters with restricted feedback. Signal Process IEEE Trans 41:649–656.

Qi S, Xu Q, Lan H, et al. (2010) Spatial distribution analysis of landslides triggered by 2008.5.12 Wenchuan Earthquake, China. Eng Geol 116:95–108. doi: 10.1016/j.enggeo.2010.07.011

Reilinger R, McClusky S, Vernant P, et al. (2006) GPS constraints on continental deformation in the Africa-Arabia-Eurasia continental collision zone and

implications for the dynamics of plate interactions. J Geophys Res 111:1–26. doi: 10.1029/2005JB004051

Reilinger RE, Ergintav S, Bürgmann R, et al. (2000) Coseismic and postseismic fault slip for the 17 August 1999, M=7.5, Izmit, Turkey. Earthq Sci 289:1519–1524.

Riedel B, Walther A (2008) InSAR processing for the recognition of landslides. Adv Geosci 189–194. doi: 10.5194/adgeo-14-189-2008

Rosen P, Henley S, Peltzer G, Simons M (2004) Updated Repeat Orbit Interferometry Package Released. Eos Trans AGU 85(5):47.

Rosen PA, Hensley S, Joughin IR, et al. (2000) Synthetic aperture radar interferometry. Proc IEEE 88:333–382. doi: 10.1109/5.838084

Sandwell DT, Myer D, Mellors R, et al. (2008) Accuracy and Resolution of ALOS Interferometry: Vector Deformation Maps of the Father's Day Intrusion at Kilauea. IEEE Trans Geosci Remote Sens 46:3524–3534. doi: 10.1109/TGRS.2008.2000634

Schulz WH (2004) Landslides mapped using LIDAR imagery. North 4:11.

Schuster RL, Highland LM (2003) Impact of landslides and innovative landslide-mitigation measures on the natural environment. Geol. Hazards Team, US Geol.

Shirzaei M (2012) A Wavelet-Based Multitemporal DInSAR Algorithm for Monitoring Ground Surface Motion. IEEE Geosci Remote Sens Lett 10:456–460. doi: 10.1109/LGRS.2012.2208935

Shirzaei M, Walter TR (2009) Randomly iterated search and statistical competency as powerful inversion tools for deformation source modeling: Application to volcano interferometric synthetic aperture radar data. J Geophys Res 114:1–16. doi: 10.1029/2008JB006071

Shirzaei M, Walter TR (2011) Estimating the Effect of Satellite Orbital Error Using Wavelet-Based Robust Regression Applied to InSAR Deformation Data. IEEE Trans Geosci Remote Sens 49:4600–4605.

Strozzi T, Ambrosi C, Raetzo H (2013) Interpretation of Aerial Photographs and Satellite SAR Interferometry for the Inventory of Landslides. Remote Sens 5:2554–2570. doi: 10.3390/rs5052554

Strozzi T, Farina P, Corsini A, et al. (2005) Survey and monitoring of landslide displacements by means of L-band satellite SAR interferometry. Landslides 2:193–201. doi: 10.1007/s10346-005-0003-2

Tan O, Taymaz T (2006) Active tectonics of the Caucasus: Earthquake source mechanisms and rupture histories obtained from inversion of teleseismic

body waveforms. Geol Soc Am Spec Pap 409:531–578. doi: 10.1130/2006.2409(25)

Tarayre H, Massonnet D (1994) Effects of a refractive atmosphere on interferometric processing. Proc IGARSS'94 717–719.

Thiebes B (2012) Landslide Analysis and Early Warning Systems. 260. doi: 10.1007/978-3-642-27526-5

Thuro K, Singer J, Festl J, et al. (2010) New landslide monitoring techniques – developments and experiences of the alpEWAS project. J Appl Geod. doi: 10.1515/jag.2010.008

Tofani V, Segoni S, Agostini A, et al. (2013) Technical Note: Use of remote sensing for landslide studies in Europe. Nat Hazards Earth Syst Sci 13:299–309. doi: 10.5194/nhess-13-299-2013

Turner AK, Schuster RL (1996) Landslides: Investigation and mitigation. 673.

Usai S (1997) The use of man-made features for long time scale INSAR. IEEE Int Geosci Remote Sens Symp Proc Remote Sens A Sci Vis Sustain Dev 4:1542–1544. doi: 10.1109/IGARSS.1997.608936

Usai S, Klees R (1999) SAR interferometry on a very long time scale: a study of the interferometric characteristics of man-made features. IEEE Trans Geosci Remote Sens 37:2118–2123.

Usai S, Klees R (1998) On the feasibility of long time scale INSAR. IEEE Int Geosci Remote Sens Symp Proc Cat No98CH36174 5:2448–2450 2754. doi: 10.1109/IGARSS.1998.702242

Vakarchuk RN, Tatevossian RE, Aptekman ZY, Bykova V V. (2013) The 1991 Racha earthquake, Caucasus: Multiple source model with compensative type of motion. Izv Phys Solid Earth 49:653–659. doi: 10.1134/S1069351313050121

Varnes DJ (1978) Slope movement types and processes. Spec Rep 176 Landslides Anal Control 11–33. doi: In Special report 176: Landslides: Analysis and Control, Transportation Research Board, Washington, D.C.

Walstra J, Chandler JH, Dixon N, Dijkstra TA (2007) Aerial photography and digital photogrammetry for landslide monitoring. Geol Soc London, Spec Publ 283:53–63. doi: 10.1144/SP283.5

Wang R, Xia Y, Grosser H, et al. (2004) The 2003 Bam (SE Iran) earthquake: precise source parameters from satellite radar interferometry. Geophys J Int 159:917–922. doi: 10.1111/j.1365-246X.2004.02476.x

Wei M, Sandwell DT (2010) Decorrelation of L-Band and C-Band Interferometry Over Vegetated Areas in California. IEEE Trans Geosci Remote Sens 48:2942–2952. doi: 10.1109/TGRS.2010.2043442 pp.2942 - 2952

Van Westen CJ, Straatsma MW, Turdukulov UD, et al. (2012) Atlas of Natural Hazards and Risk in Georgia. CENN Caucasus Environmental NGO Network

Xia Y (2008) CR-Based SAR-Interferometry for Landslide Monitoring. IGARSS 2008 - 2008 IEEE Int. Geosci. Remote Sens. Symp. IEEE, pp II–1239–II–1242

Zebker HA, Rosen PA, Hensley S (1997) Atmospheric effects in interferometric synthetic aperture radar surface deformation and topographic maps. Geophys Res 102:7547–7563.

Zebker HA, Villasenor J (1997) Decorrelation in interferometric radar echoes. IEEE Geosci Remote Sens 30:950–959.